nature communications

Article

https://doi.org/10.1038/s41467-026-76015-3

ERH elicits cell lineage restriction in mammalian preimplantation development and differentiation from pluripotency via H3K9me3-heterochromatin

Received: 28 January 2025

Accepted: 7 July 2026

Published online: 30 July 2026

Check for updates

Andrew Katznelson[1], Blake Hernandez[1], Kylea Tapia[2], Holly Fahning[2], Adam Burton[3], Jingchao Zhang[1], Maria-Elena Torres-Padilla[3,4], Nicolas Plachta[1], Kenneth S. Zaret[1] & Ryan L. McCarthy[2,5]

Enhancer of Rudimentary Homolog (ERH) is an evolutionarily conserved protein originally characterized as promoting fission yeast heterochromatin and recently shown to maintain H3K9me3 heterochromatin in human fibroblasts. Here, we find that ERH depletion in fibroblasts reverts the somatic cell H3K9me3 landscape of broad megabase size domains to an embryonic stem cell (ESC) state composed of mainly H3K9me3 peaks and enables activation of naïve and pluripotency genes and transposable elements during induced pluripotent stem cell (iPSC) reprogramming. Concordantly, we find that ERH represses totipotent and alternative lineage programs during mouse preimplantation development and is required for proper segregation of the inner cell mass and trophectoderm cell lineages. During human ESC differentiation into germ layer lineages, ERH silences naïve and pluripotency genes, transposable elements, and alternative lineage somatic genes. As in fission yeast, we find that mammalian ERH interacts with RNA-binding proteins to engage and repress its chromatin targets. Our findings reveal a conserved, fundamental role for ERH in mammalian cell fate specification via the initiation and maintenance of early developmental gene repression.

Heterochromatin marked by histone H3 lysine 9 trimethylation (H3K9me3) represses the expression of many protein-coding genes and DNA repeat elements[1–3]. Yet despite its stability, H3K9me3-heterochromatin is dynamically established, maintained, and rearranged during embryogenesis[1,4,5]. Zygotic genome activation (ZGA), marked by the initial transcription of key genes and transposable elements[6], occurs at the 1-2 cell stage in mice and the 4-8 cell stage in humans[6] and requires demethylation of maternal H3K9me3 marks created in oocytes[7,8]. As the embryo loses totipotency and differentiates into the first two developmentally-specified lineages, the trophectoderm of the blastocyst and the inner cell mass (ICM), many ZGA-specific protein-coding genes and repeats gain H3K9me3 and are subsequently silenced[4,9,10]. As development proceeds, H3K9me3 is further established on lineage-inappropriate genes and repeat elements[4,9,11], with the highest number of genes marked by H3K9me3 at the germ-layer stage[1]. Throughout germ layer specification to mature

[1]Institute for Regenerative Medicine and Department of Cell and Developmental Biology, Perelman School of Medicine, University of Pennsylvania, Philadelphia, PA, USA. [2]Center for Developmental Biology and Regenerative Medicine, Seattle Children's Research Institute, Seattle, WA, USA. [3]Institute of Epigenetics and Stem Cells (IES), Helmholtz Zentrum München D-81377, München, Germany. [4]Faculty of Biology, Ludwig-Maximilians Universität, München, Germany. [5]Department of Pediatrics, University of Washington School of Medicine, Seattle, WA, USA. e-mail: zaret@pennmedicine.upenn.edu; Ryan.McCarthy@seattlechildrens.org

somatic lineages, H3K9me3 is removed from genes that become active and is deposited onto early developmental genes that become repressed[1]. The H3K9me3 landscape changes substantially from pluripotency to early and terminally differentiated states[12,13]. The mechanisms operating in the initial targeting of histone methyltransferases to deposit H3K9me3 and the maintenance of the initially established H3K9me3 domains remain poorly understood. In this study, we compared how the enhancer of rudimentary homolog (ERH), a highly conserved heterochromatin protein distinct from histone methyltransferases, contributes to H3K9me3 dynamics and gene repression in differentiated somatic cells, pluripotent cell lines, and early mammalian development.

ERH is an evolutionarily conserved protein originally discovered in fission yeast to regulate sporulation, the primary form of yeast cell differentiation, via H3K9 methylation[14,15]. In *S. pombe*, Erh1 forms a complex with the RNA-binding protein Mmi1, which is recruited by binding of nascent meiotic transcripts through its YTH domain[14,15]. Erh1-Mmi1 then causes the degradation of its bound RNA transcripts, the establishment of H3K9 methylation, and consequent repression of meiotic and developmental genes, transposons, and rDNA[14,15]. We recently found that in terminally-differentiated primary human fibroblasts, ERH is highly enriched in H3K9me3-heterochromatin, where it represses meiotic and germ cell genes, similar to that observed in fission yeast[3,14,16]. We further found that ERH in mammals has evolutionarily expanded its function to include the majority of regions that exhibit H3K9me3 heterochromatin in somatic cells, including alternative-lineage protein-coding genes and repeat elements[16]. While ERH is highly conserved among eukaryotes, its fission yeast partner Mmi1 lacks a metazoan homolog[17]. Thus, how cell-type-specific cofactors recruit ERH to chromatin to regulate cell identity throughout mammalian development is unknown.

Here, we find that upon ERH loss in fibroblasts, there is reversion to a pluripotency-like H3K9me3 state, which is permissive to binding of pluripotency transcription factors, which in turn activate pluripotency and alternative lineage genes and repeat elements. The derepression of pluripotency and alternative lineage programs led us to investigate the role of ERH in the earliest developmental stages, where repression by H3K9me3 has been implicated during trophectoderm and inner cell mass segregation in the blastocyst[4,9,10] and the differentiation from pluripotency to the germ layer lineage[1]. By genetic perturbation, chromatin and gene expression profiling, and imaging, we identify a role for ERH across mouse and human systems in repressing early naïve pluripotency and alternative lineage genes. We find that targeting of mammalian ERH to chromatin occurs through cell-type-specific interactions with RNA-binding proteins, enabling context-dependent functions. Together, our findings demonstrate a fundamental role for ERH during developmentally acquired H3K9me3-mediated gene repression and maintenance of such repression in somatic cells.

Results

ERH depletion in primary human fibroblasts causes H3K9me3 to revert to an ESC-like state

We assessed how H3K9me3 is disrupted after ERH loss by CUT&RUN for H3K9me3 after siRNA knockdown in human primary fibroblasts (Fig. 1a). Consistent with our previous study[16], we confirmed that H3K9me3 is globally reduced in human fibroblasts after ERH knockdown (Fig. 1b). Yet while large megabase-scale domains were diminished (Fig. 1c top, purple domains in top two tracks), as seen previously[16], 10,526 H3K9me3 residual peaks were retained in the ERH knockdown (Fig. 1c, lower, second track) and Supplementary Data 1). Remarkably, the residual H3K9me3 peaks in siERH fibroblasts resemble the H3K9me3 profile in H1 ESCs (Fig. 1c lower, third track). Across the genome, 85% of the residual fibroblast siERH H3K9me3 sites overlap with H3K9me3 peaks in H1 hESCs (Supplementary Fig. 1a). Pearson correlation of H3K9me3 peaks from fibroblasts after siControl or siERH, as well as in hESCs, supports a shift in the H3K9me3 heterochromatin landscape to an embryonic state (Fig. 1d,e). Thus, while loss of ERH in primary fibroblasts causes a global loss of H3K9me3 domains, embryonic H3K9me3-marked genomic sites are retained.

We hypothesized that since ERH depleted fibroblasts retain hESC-like H3K9me3 peaks (Fig. 1c-e), ERH may be dispensable for maintaining H3K9me3 in hESCs. To test this hypothesis we depleted ERH in H1 hESCs cultured in pluripotency-maintaining conditions, which caused no observable changes in colony morphology or loss of pluripotency (Fig. 1f), even after sustained knockdown (Supplementary Fig. 1d). H3K9me3 level and nuclear organization by immunofluorescence was not changed in siERH-treated hESCs (Fig. 1g; Supplementary Fig. 1e). We also observed no change in H3K27me3 (Supplementary Fig. 1f). Despite no apparent disruption of the pluripotent state or global H3K9me3 levels, ERH-depleted hESCs show an increased nuclear area and nuclear blebbing (Supplementary Fig. 1g), which are changes associated with chromatin decompaction[18]. We previously found that ERH depletion did not change the expression or protein level of H3K9me3 HMTs[16], we similarly observe no significant decrease in H3K9me3 HMT expression upon ERH depletion in pluripotent hESCs (Supplementary Fig. 1h). To investigate potential locus-specific changes in hESC H3K9me3 upon ERH depletion, we conducted H3K9me3 CUT&RUN in siControl and siERH-treated hESCs. Consistent with our immunofluorescence results, we observed minimal change in H3K9me3 (Supplementary Fig. 1i) and high correlation between H3K9me3 peaks in siControl and siERH-treated hESCs (Supplementary Fig. 1j).

To identify chromatin-associated proteins and pathways regulating the residual H3K9me3 peak sites in human fibroblasts, we analyzed the regions using the cistromeDB Toolkit, which uses a compendium of published ChIP-seq data sets[16,17]. We find that most proteins enriched at the residual peak sites in ES cells (i.e., prior to ERH knockdown) are either KRAB-ZNFs or involved in H3K9me3 repression via KAP1, which is recruited to chromatin through binding the KRAB domain (Fig. 1h)[19]. Likewise, de novo motif analysis finds that enriched sequence motifs in the residual peak sites are for KRAB-ZNF factors (Supplementary Fig. 1k). Consistent with the enrichment analysis, the residual siERH H3K9me3 peak sites are highly enriched for H3K9me3, KAP1, and HP1 in ES cells (Fig. 1e, i and Supplementary Fig. 1l). As KRAB-ZNFs repress transposons via H3K9me3, we hypothesized the residual peaks would be enriched over repeats. Repeat enrichment analysis found that the residual peaks are enriched over canonical KRAB-ZNF targets: LINEs, LTRs, and satellite repeats (Supplementary Fig. 1m). We conclude that ERH is required to maintain the broad H3K9me3 domains that are established over the course of development and are present in terminally differentiated cells, but does not control H3K9me3 peaks attributed to the DNA-dependent association of KAP1 that persists from pluripotency over constitutively repressed repeats.

ERH-dependent H3K9me3 suppresses SOX2 binding and activation of pluripotency genes and repeats during OSKM reprogramming

H3K9me3 impairs induced pluripotent stem cell (iPSC) reprogramming by blocking transcription factor binding, and pluripotency genes marked by H3K9me3 show delayed activation compared to genes in heterochromatin marked with H3K27me3 or neither mark (Supplementary Fig. 2a)[20]. To test whether ERH-dependent H3K9me3 contributes to this barrier, we depleted ERH by siRNA prior to OSKM induction and assessed transcription factor binding and gene activation at 48 h of reprogramming (Fig. 1a and Supplementary Data 2–4), as H3K9me3 is inhibitory to transcription factor activity at this stage[20]. Immunofluorescence confirmed that both ERH and H3K9me3 are effectively depleted at this time point, with H3K9me3 loss persisting through 11 days after the second siRNA treatment, before recovering (Supplementary Fig. 2b).

https://doi.org/10.1038/s41467-026-76015-3

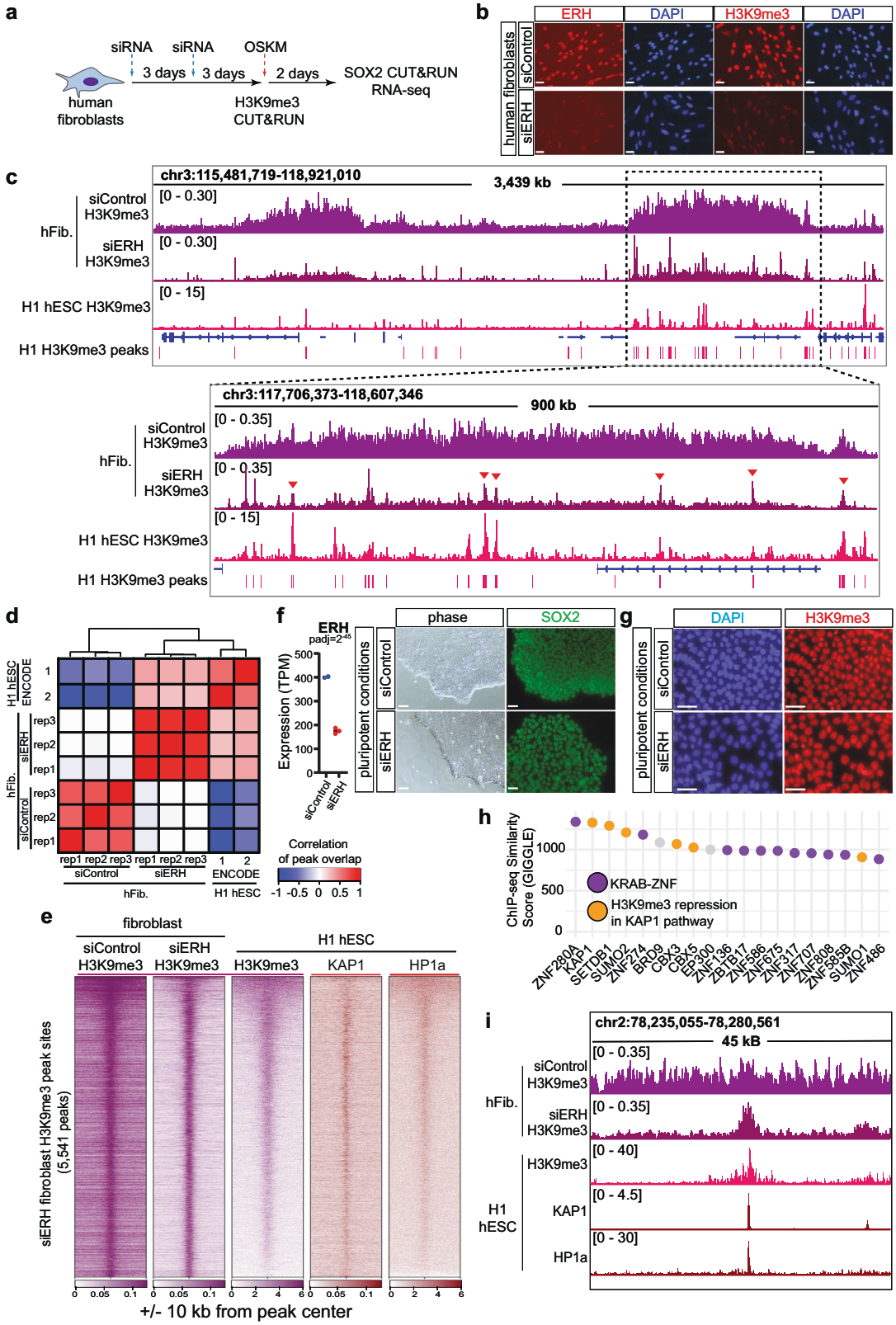

CUT&RUN of SOX2 after 48 h of OSKM reprogramming of fibroblasts showed that while most binding sites were shared between siControl and siERH fibroblasts, 2,538 binding sites were gained (Supplementary Fig. 3a and Supplementary Data 2). We observed that ERH knockdown enabled SOX2 to target loci in fibroblasts that lose H3K9me3, including within heterochromatin domains previously annotated as resistant to reprogramming factor binding[20] (Fig. 2a and Supplementary Fig. 3b–d). By assessing the genomic locations of siERH-gained SOX2 peaks in the cistromeDB toolkit[21,22], we found that the newly gained SOX2 sites had the most similarity to ChIP-seq peak sets of SOX2 and its pluripotency partners NANOG and OCT4 in embryonic stem cells (Supplementary Fig. 3e). Inspection of genome browser tracks identified specific loci where loss of ERH-controlled H3K9me3 enabled SOX2 binding over normal SOX2 and NANOG

Fig. 1 | ERH depletion reverts fibroblast H3K9me3 patterns to an hESC-like state. a Schematic of siRNA treatments and timing for H3K9me3 CUT&RUN experiments shown in Fig. 1 and SOX2 CUT&RUN and RNA-seq experiments shown in Fig. 2. **b** Immunofluorescence of ERH (red), H3K9me3 (red) and DAPI (blue) in siControl and siERH human fibroblasts. Scale bars, 50 μm. $N = 3$ biological replicates. **c** Browser track of H3K9me3 levels in siControl and siERH treated human fibroblasts and H1 hESCs (GSM1003585) at the megabase-domain level and gene level. Example H3K9me3 peaks common between siERH fibroblasts and H1 hESCs are indicated by red triangles. **d** Heatmap of fibroblast siControl and siERH H3K9me3, H1 hESC H3K9me3 (GSM1003585) and H1 hESC HP1α (GSE123229) levels centered at siERH retained H3K9me3 peaks located within fibroblast H3K9me3 domains ±10 kb. **e** Correlation of H3K9me3 from BJ fibroblasts after siControl or siERH with H1 hESC H3K9me3. **f** Graph of ERH expression by RNA-seq from siControl and siERH H1 hESCs. Differential expression was assessed by DESeq2 (two-sided Wald test with Benjamini–Hochberg adjustment for multiple comparisons), $n = 2$ for siControl $n = 3$ for siERH). Representative images showing hESC morphology and SOX2 (green) pluripotency marker staining in siControl and siERH H1 hESCs under pluripotency maintaining conditions. Scale bars, 50 μm. $N = 3$ biological replicates. **g** Representative images of H3K9me3 (red) and DAPI (blue) in siControl and siERH H1 hESCs under pluripotency maintaining conditions. Scale bars, 50 μm. $N = 3$ biological replicates. **h** CistromeDB Toolkit enrichment analysis of fibroblast siERH H3K9me3 peaks. The top 20 proteins scored by the analysis are visualized. Proteins colored by characterization as H3K9me3-associated (orange), KRAB zinc-finger transcription factors (purple), and euchromatin-associated (gray). **i.**Browser track comparing siControl and siERH fibroblast H3K9me3 with H1 hESC H3K9me3 (GSM1003585) and HP1a (GSM1701825) patterns. Peak locations called by SEACR analysis on siERH H3K9me3 data are shown. See also Supplementary Fig. 1 and Supplementary Data 1. Source data are provided as a Source Data file.

targets in ES cells (Fig. 2b and Supplementary Fig. 3f). We next assessed if loss of ERH-dependent H3K9me3 enables other transcription factors to bind previously refractory sites . By performing CUT&RUN footprinting of SOX2's primary binding cofactors during reprogramming, KLF4 and OCT4, we found enhanced footprints for each factor at SOX2 sites gained by siERH (Supplementary Fig. 3g). Thus, ERH loss during pluripotency reprogramming enables pluripotency transcription factor binding in what were heterochromatic H3K9me3 regions in fibroblasts.

Protein coding genes embedded in H3K9me3 domains, normally refractory to transcription factor activation, were activated after siERH (136 up, 13 down; Fig. 2c). Significantly, genes associated with the human 8-cell like cell (8CLC) state[23] were activated, including *ZSCAN4, DUXA, DPPA4, LIN28A, TPRXL*[24]*, KLF5*, and the histone variant *H3.Y*[25] (Fig. 2d and Supplementary Fig. 4a). We compared the activation levels of these genes in siERH+OSKM with existing RNA-seq datasets[26] and found that *H3.Y, DUXA*, and *TPRXL* do not normally get activated at levels similar to siERH+OSKM at any stage during iPSC reprogramming (Supplementary Fig. 4b). However, activation of 8CLC genes in siERH +OSKM is incomplete, as many genes activated in naïve ESCs[27] are not expressed or expressed at lower levels in siERH+OSKM (Supplementary Fig. 4c), suggesting low activation of naïve programs but not full conversion to a naïve cell state. While the activation of marker genes such as DUXA and ZSCAN4 was lower than in 8C embryos (Supplementary Fig. 4d)[28], we conclude that ERH-dependent H3K9me3 safeguards early totipotent and pluripotent genes and that ERH loss creates a permissive environment for transcription factor binding and activation.

We observed that *LTR7* and *HERVH* repeats, which are expressed in and required to maintain pluripotency[29,30], lose H3K9me3 after ERH depletion and are activated in siERH+OSKM (Fig. 2e). *LTR7Y* repeats, which promote naïve pluripotency[31], exhibited similar ERH-dependent H3K9me3 and repression (Fig. 2f, g and Supplementary Fig. 4e). Notably, residual H3K9me3 peaks retained at *LTR7Y* repeats were insufficient to maintain repression (Fig. 2f, g). Global analysis of genes with transcription start sites withing 25 kb of LTR7Ys revealed that genes proximal to LTR7Ys with high (log2fc > 2) activation upon ERH depletion exhibited higher gene activation while both sets of genes showed similar loss of H3K9me3 (Supplementary Fig. 4f), suggesting that activation of ERH repressed repeat elements may portent expression of nearby genes. Furthermore, we observed activation of repeat elements that function specifically during the human 8 cell-like cell stage and are later marked by H3K9me3 and silenced in the human blastocyst[4] (Supplementary Fig. 4g). These results demonstrate that ERH maintains H3K9me3 repression of a subset of 8-cell stage and pluripotency repeats in terminally differentiated human cells.

Depletion of H3K9me3 HMTs has been shown to increase iPSC reprogramming[20]. However, despite increased activation of pluripotency and 8-cell genes at 48 h after initiation of OSKM-based iPSC reprogramming in siERH treated fibroblasts, by day 2 we observed substantial cell death that persisted 7 days into reprogramming, past the initial apoptotic wave (Supplementary Fig. 4h, i) and resulting in no iPSC colonies forming in siERH+OSKM conditions, compared to the abundant colonies in siControl+OSKM conditions (Supplementary Fig. 4j, k). The failure to generate iPSC colonies was not rescued by simultaneous knockdown of p53 (Supplementary Fig. 4k). Lower ERH siRNA decreased cell death, but did not change the emerging iPSC colony number (Supplementary Fig. 4i, j). Using XDeathDB[32] on our RNA-seq data identified increased expression of genes activated in several cell death pathways, including RIPK2 signaling (Supplementary Fig. 4l). We investigated if simultaneous inhibition of RIPK2 along with inhibition of RIPK3 and Caspases 3 and 7, which has been shown to improve survival of cells activating 8-cell like genes[23], could enable survival of siERH+OSKM iPSCs. Notably, we found that adding small molecule inhibitors GSK2983559, Ac-DEVD-CHO, and GSK872 to inhibit RIPK2, Caspases 3 and 7, and RIPK3, respectively, enabled the generation of iPSC colonies with ERH depletion at a significantly higher efficiency compared to siControl (Supplementary Fig. 4m). RIPK2 inhibition alone was necessary and sufficient to successfully generate iPSC colonies expressing pluripotency factors during ERH depletion, while inhibition of RIPK and Caspases 3 and 7 was not sufficient but did increase colony size (Supplementary Fig. 4n). These findings demonstrate that the increased accessibility for transcription factor binding in H3K9me3 domains (Fig. 2a, b) and improved activation of the pluripotency network (Fig. 2c, d) observed upon ERH depletion can increase iPSC reprogramming efficiency.

ERH is necessary for trophectoderm development, the first embryonic differentiation

Our finding that ERH represses naïve genes normally expressed in 2-8 cell embryos in fully differentiated fibroblasts led us to investigate whether ERH establishes silencing of 2-8 cell genes during pre-implantation development. We first analyzed existing RNA-seq data of mouse embryogenesis timepoints from zygote to blastocyst[33] and found that ERH mRNA is present across pre-implantation development and is significantly increased from the 8-cell stage through the blastocyst stage (Supplementary Fig. 5a). Immunostaining mouse embryos for ERH protein at the zygote, 2-cell, 8-cell and blastocyst stages revealed that, consistent with its mRNA levels, ERH is expressed and nuclear-localized at all stages analyzed, with increasing abundance in the early and late blastocyst stages (Fig. 3a, b). At the blastocyst stage, ERH levels are similar in ICM and trophectoderm cells (Supplementary Fig. 5b).

To investigate if ERH is involved in pre-implantation lineage specification, we depleted ERH levels by siRNA micro-injection at the 1-cell stage of mouse embryos, compared to a nontargeting siRNA control, and assessed impacts on the blastocysts (Supplementary Fig. 5c). ERH depletion did not cause major morphological changes in blastocyst structure, as both siControl and siERH blastocysts form a cavity and segregate ICM and trophectoderm cells (Supplementary Fig. 5c, d). Staining blastocysts for key transcription factors involved in lineage

https://doi.org/10.1038/s41467-026-76015-3

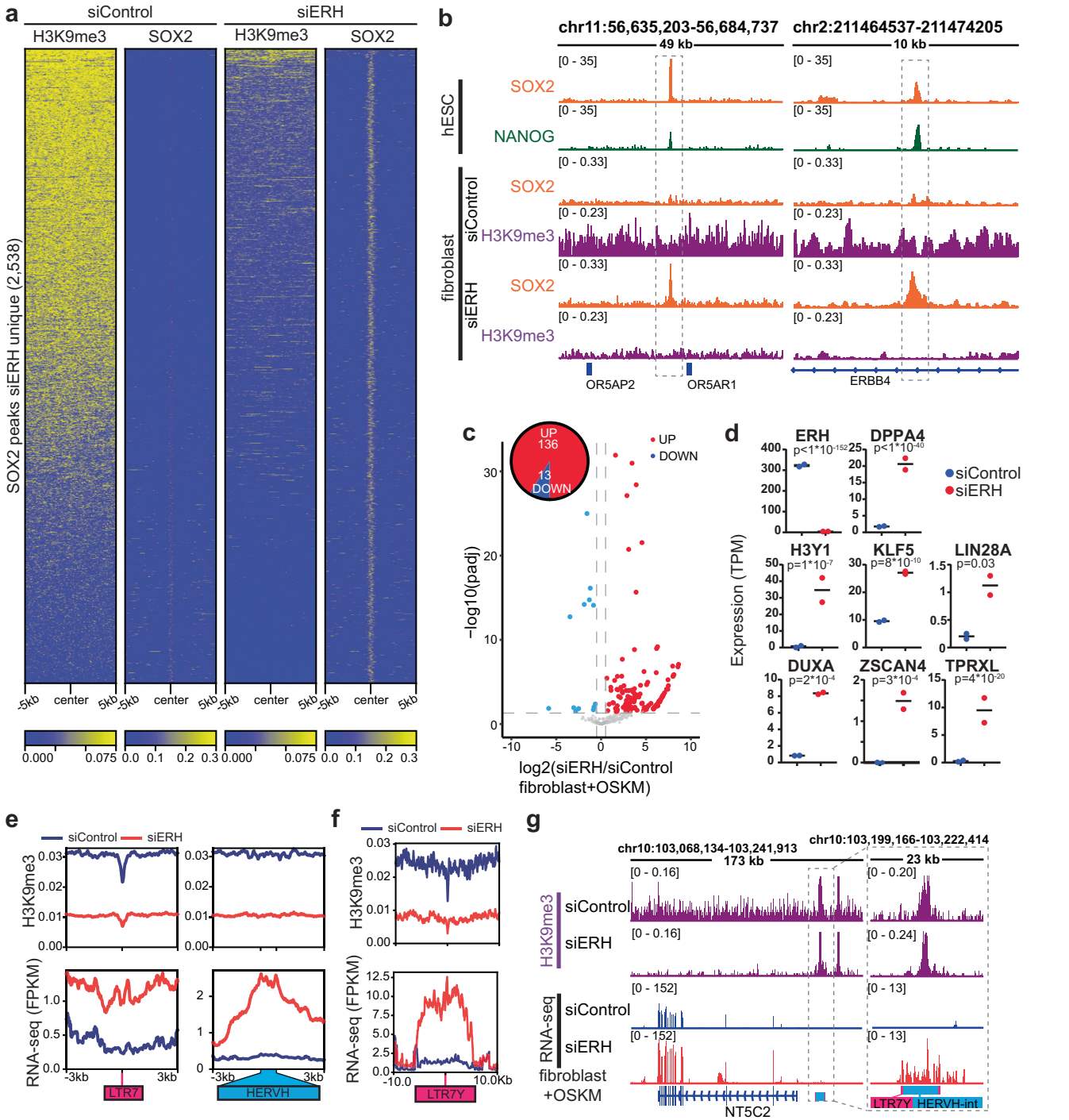

Fig. 2 | ERH depletion enhances gene activation of pluripotency and alternative lineage genes during iPSC reprogramming. a Heatmap of H3K9me3 CUT&RUN from siControl and siERH human fibroblasts and SOX2 CUT&RUN from siControl and siERH fibroblasts+OSKM at siERH-gained SOX2 peaks. **b** Browser track of example hESC SOX2 and NANOG peak coincident with fibroblast siERH H3K9me3 loss and SOX2 peak gain. **c** Volcano plot of expression changes in siERH vs siControl fibroblasts+OSKM of iPSC activated genes located in fibroblast H3K9me3 domains. Differential expression was assessed by DESeq2 (two-sided Wald test with Benjamini–Hochberg adjustment for multiple comparisons) **d** Expression of ERH and example naïve pluripotency genes activated in 48 h OSKM by ERH depletion. Transcripts per million (TPM) values from RNA-seq replicates shown; Differential expression was assessed by DESeq2, adjusted p-value reported (two-sided Wald test with Benjamini–Hochberg adjustment for multiple comparisons). **e** Profile plots of H3K9me3 and RNA levels from LTR7 and HERVH repeats in siERH vs siControl fibroblasts+OSKM. **f** Profile plots of H3K9me3 and RNA levels from LTR7Y repeats in siERH vs siControl fibroblasts+OSKM. **g** Browser track showing H3K9me3 in siControl and siERH fibroblasts and RNA levels in siControl+OSKM and siERH +OSKM for gene and adjacent LTR7Y naïve pluripotency repeat. See also Supplementary Fig. 2–4 and Supplementary Datas 2–4. Source data are provided as a Source Data file.

https://doi.org/10.1038/s41467-026-76015-3

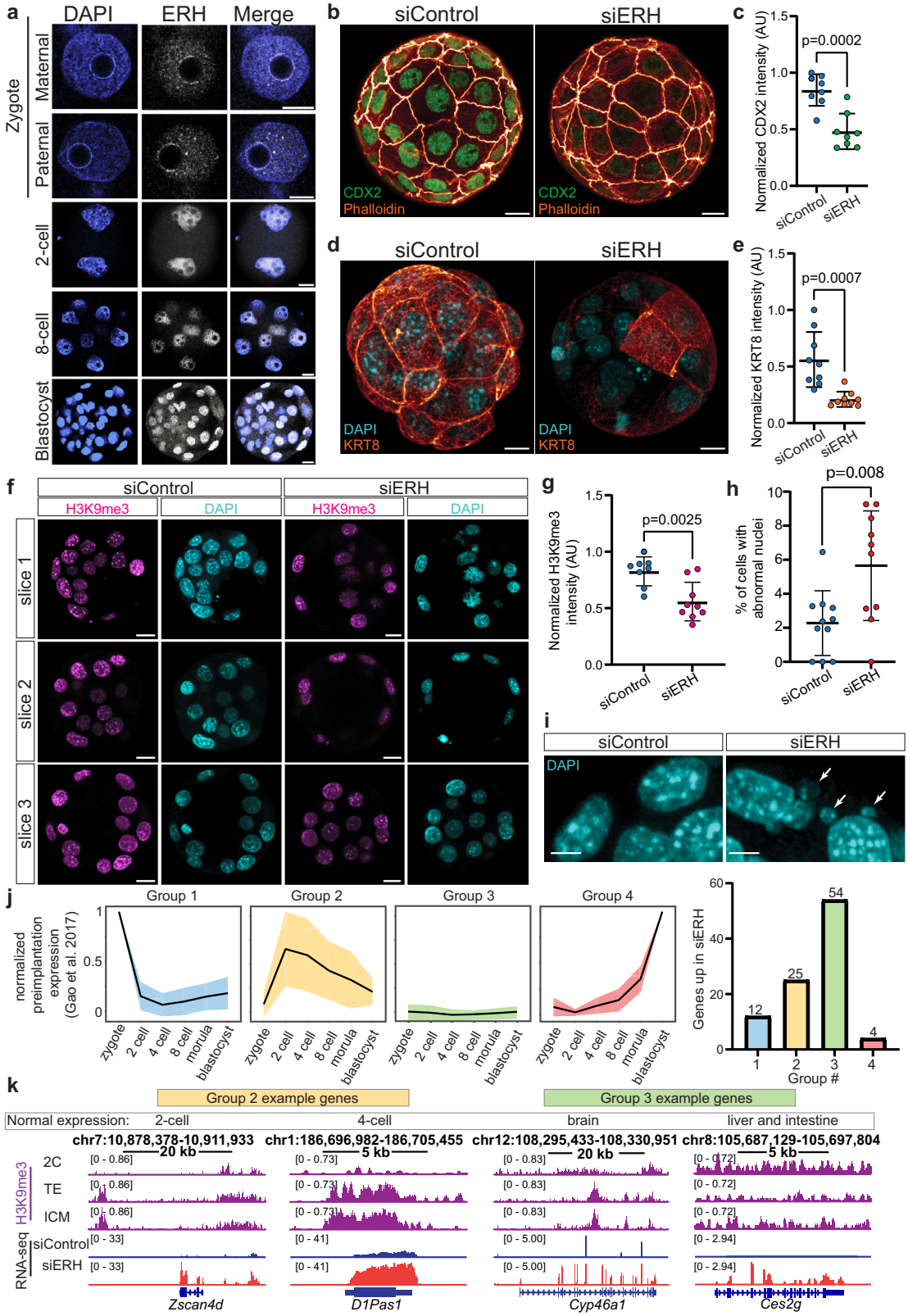

specification revealed similar levels of the pluripotency marker OCT4 in ICM and TE cells between siControl and siERH blastocysts (Supplementary Fig.5e). However, the levels of the trophectoderm-determining transcription factor CDX2[34] (Fig. 3b, c) and the trophectoderm marker Keratin 8[35] (Fig. 3d, e) were significantly decreased in the ERH-depleted blastocysts. Thus, ERH is required for proper trophectoderm differentiation.

The role of ERH in H3K9me3 heterochromatin regulation in *S. pombe*[14,15] and human fibroblasts[16] suggests that defects in trophectoderm differentiation may arise from alterations in gene silencing mechanisms. Indeed, we observed a 32% decrease ($p = 0.0025$) in H3K9me3 by immunofluorescence in blastocysts of ERH-depleted embryos (Fig.3f, g and Supplementary Data 5). We also observed a significant increase in nuclear DNA shedding in the siERH blastocysts

Fig. 3 | ERH is expressed during pre-implantation mouse development and is critical for normal blastocyst development by repressing 2-cell and alternative lineage genes. a ERH (white) and DAPI (blue) staining during mouse pre-implantation development. Representative confocal z-sections are shown (zygote $n = 15$, $N = 3$, 2-cell stage $n = 18$, $N = 3$, 8-cell stage $n = 6$, $N = 2$, blastocyst $n = 10$, $N = 3$). Scale bars, 10 μm. **b** Representative images of trophectoderm marker Cdx2 (green) in siControl and siERH blastocysts with Phalloidin (orange) marking cell boundaries. Scale bars, 10 μm. **c** Quantification of CDX2 intensity in siControl vs siERH blastocysts. Data are presented as mean values ± SD; statistical comparison was performed using a two-sided unpaired *t*-test; $n = 8$ (siControl) and $n = 8$ (siERH) blastocytes examined. **d** Representative image of trophectoderm marker KRT8 (orange) in siControl and siERH blastocysts with DAPI (blue). Scale bars, 10 μm. **e** Quantification of KRT8 intensity in siControl vs siERH blastocysts Data are presented as mean values ± SD; statistical comparison was performed using a two sided unpaired *t*-test; $n = 8$ (siControl) and $n = 9$ (siERH) blastocytes examined. **f** Representative images of H3K9me3 (magenta), DAPI (teal) in siControl vs siERH blastocysts. Scale bars, 10 μm. **g** Quantification of H3K9me3 level in siControl vs siERH blastocysts. Data are presented as mean values ± - SD; statistical comparison was performed using a two-sided unpaired *t*-test; $n = 8$ (siControl) and $n = 9$ (siERH) blastocytes examined. **h** Percentage of cells per blastocyst with abnormal nuclei. Data are presented as mean values ± SD; statistical comparison was performed using a two-sided unpaired *t*-test; $n = 11$ (siControl) and $n = 9$ (siERH) blastocytes examined. **i** Representative image of DAPI staining siCTRL and siERH blastocysts with white arrows indicating DNA shedding. Scale bars, 5 μm. **j** ERH repressed blastocyst genes (adjusted *p*-value < =0.05, log2fc > =0.5) grouped based upon normal expression patterns exhibited during mouse pre-implantation development re-analyzed from Gao et al., 2017[33]. Black lines indicate mean scaled expression; shaded ribbons represent standard deviation. **k** Example gene tracks of genes significantly upregulated in siERH vs siControl blastocysts (adjusted *p*-value < =0.05, log2fc > =0.5, $n = 3$) with H3K9me3 tracks for 2 cell, trophectoderm and ICM cells from ref. 9. See also Supplementary Fig. 5 and Supplementary Datas 5,6. Source data are provided as a Source Data file.

(Fig. 3h, i and Supplementary Fig. 5f), similar to the observed nuclear DNA shedding in siERH hESCs (Supplementary Fig. 1g). Decreased keratin levels as observed in siERH blastocysts (Fig. 3d, e) have been shown to make trophectoderm cells of blastocysts more susceptible to DNA shedding[36], as has decreased H3K9me3[18].

To characterize how these changes impact gene expression, we performed RNA-seq on mouse blastocysts 4 days after injecting siControl or siERH at the 1-cell stage (Supplementary Data 6), which confirmed an ~80% knockdown of ERH (Supplementary Fig. 5g). We classified genes upregulated in ERH-depleted blastocysts into 4 groups, based upon their expression during normal mouse pre-implantation development[33] (Fig. 3j; Supplementary Data 7). Group 1 consists of transcripts present at the zygote stage, including maternally inherited transcripts, that become silenced or degraded as development progresses. Group 2 consists of transcripts that are highly expressed in the 2-8-cell stages and low or absent in the zygote and blastocyst stage. Group 3 consists of transcripts that are absent or lowly expressed at all stages measured. Group 4 consists of transcripts with the highest expression in the blastocyst stage. Of the ERH-repressed genes (i.e., genes whose expression goes up upon ERH knockdown), 25 normally have peak expression during the 2-8-cell stage (group 2) and 54 are normally not expressed during pre-implantation development (group 3). ERH-repressed group 2 genes included the 2-cell specific *Zscan4d* [37] and the 4-cell specific *D1Pas1*[38] (Fig. 3k). ERH-repressed group 3 alternative lineage genes included genes specific to the brain[39], liver, and intestine[40] (Fig. 3k).

Comparing our RNA-seq data with existing mouse preimplantation H3K9me3 ChIP-seq data[9], we found that the genes repressed by ERH at the 2-cell stage and later, alternative lineage genes were initially marked by H3K9me3 (Fig. 3k). We further found that upon ERH depletion, key markers of primitive endoderm, including *Gata4* and *Sox17*[41], were significantly repressed (Supplementary Fig. 5h), while epiblast genes were unchanged (Supplementary Fig. 5i). We conclude that ERH is necessary to silence 2–8-cell stage genes and prevent the spontaneous activation of later developmental genes during the blastocyst stage, and that failure to silence results in improper lineage specification in the blastocyst.

ERH is necessary for proper lineage commitment and restriction during human ESC differentiation

Our finding that ERH is critical for blastocyst development led us to ask if ERH depletion impacted the ability of hESCs to differentiate. When we used Activin A and the GSK-3 Inhibitor CHIR99021 together to differentiate hESCs to an endoderm identity[42], as expected within 24 hours we observed repression of pluripotency factors and initial expression of endodermal markers in a subset of cells (Supplementary Fig. 6a). Yet depletion of ERH in H1 hESCs followed by 24 h endoderm differentiation showed a failure to decrease NANOG protein levels (Fig. 4a and Supplementary Fig. 6b) and reduced emergence of SOX17+ cells (Fig. 4a). To assess if this observation was specific to endoderm, we also performed differentiation to ectoderm with control and ERH depleted cells for 2 days with retinoic acid treatment. We observed sustained expression of the pluripotency factor OCT4 and decreased abundance of the ectodermal transcription factor PAX6 (Fig.4b).

To investigate transcriptional changes caused by ERH depletion, we performed RNA-seq of siRNA control and ERH depleted H1 hESCs (Supplementary Fig. 6c and Supplementary Data 8), and after 1 day of endoderm or 2 days of ectoderm differentiation. Loss of ERH in hESCs caused widespread gene dysregulation (Supplementary Fig. 6d, Supplementary Data 8), consistent with ERH having roles independent of H3K9me3 maintenance in hESCs (Fig. 1). Genes normally repressed in the siControl endoderm and ectoderm differentiation were preferentially upregulated by ERH depletion (endoderm, Supplementary Fig. 6f; ectoderm Supplementary Fig. 6g).

During endoderm differentiation, we observed that ERH depletion preferentially upregulated genes identified as higher in naïve vs primed hESCs[43] (Supplementary Fig. 6h), beyond what was observed in the pluripotent state (Supplementary Fig. 6e). For example, the gene for the pluripotency factor NANOG, previously demonstrated to be repressed by H3K9me3 during pluripotency exit[44], was significantly upregulated by ERH depletion (Fig. 4c), consistent with our immunostaining (Fig. 4a and Supplementary Fig. 6b). Additionally, genes found to be expressed in human pluripotent stem cells were upregulated during endoderm and ectoderm differentiation after ERH depletion, including *DUSP5/6, NODAL, LEFTY1/2*, and *DACT1* (Supplementary Fig. 6i and Supplementary Data 8). Genes associated with the 2-cell stage and naïve pluripotency, including *ZSCAN4*[37], *KLF5*[31], *ESRRB*[45], *NR5A2*[46] and *NANOGP1*[47], were upregulated during siERH-treated hESC differentiation (Fig. 4d and Supplementary Fig. 6j). The expression of naïve genes after ERH depletion was at a much lower level than in true naïve hESCs (Supplementary Fig. 6k), indicating permissive expression but not spontaneous primed to naïve conversion. We conclude that ERH is required to repress pluripotency genes during hESC pluripotency exit.

During differentiation, a key function of H3K9me3 heterochromatin is to repress alternative lineage genes[1,9]. Our finding that ERH depletion in blastocysts upregulates lineage-incompatible genes (Fig. 3j, k) led us to investigate if a similar consequence occurs during hESC differentiation. GO analysis of genes upregulated by ERH depletion during endoderm and ectoderm differentiation confirmed activation of transcriptional networks typically not induced by the specific differentiation treatment (Fig. 4e, Supplementary Fig. 7a, and Supplementary Data 10). ERH depletion upregulated meiotic and gametogenic genes in all tested developmental stages (Supplementary Fig. 7b), consistent with previous findings in human fibroblasts[16] and

https://doi.org/10.1038/s41467-026-76015-3

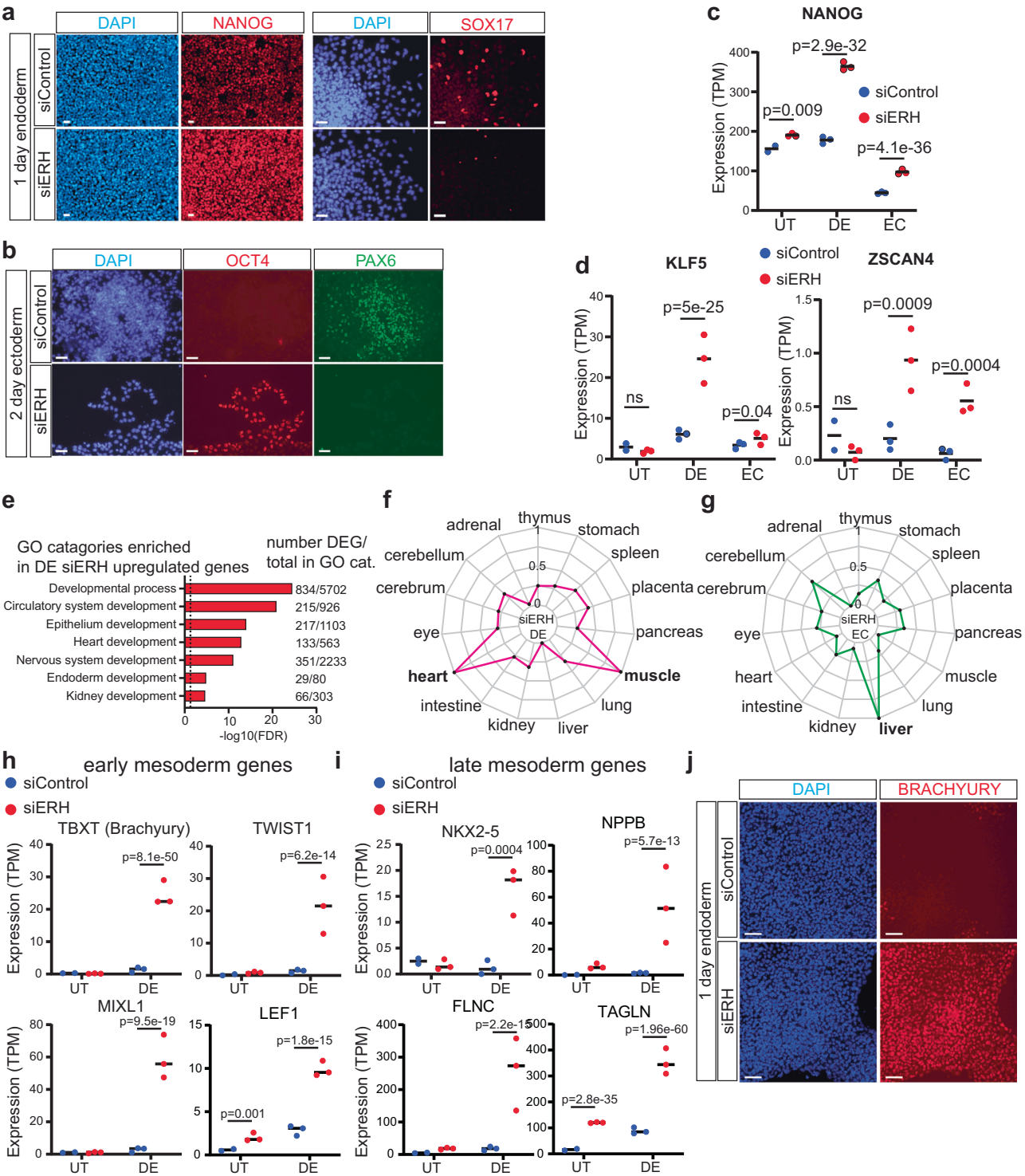

the role of Erh1 in *S. pombe* sporulation[14]. To further assess the cell lineages in which the upregulated genes function, we generated composite expression profiles of the genes upregulated by ERH depletion during endoderm (Fig. 4f) and ectoderm differentiation (Fig. 4g) from expression data downloaded from the BBI Descartes human single cell atlas[48], and found that heart, muscle and liver genes are preferentially activated. Directed differentiation of hESCs to endoderm[42], instead induced both early and late mesodermal genes[49] when ERH was depleted (Fig. 4h, i). Notable inappropriate gene activation in siERH definitive endoderm included *NXK2-5, NPPB* and *FLNC*, typically expressed in heart muscle, as well as *TAGLN*, a canonical smooth muscle marker (Fig. 4i). Increased levels of BRACHYURY protein, a key determinant of early mesoderm[50], was also confirmed by immunofluorescence (Fig. 4j). Inappropriate activation during ectoderm differentiation with ERH knockdown included genes typically expressed in liver development (Supplementary Fig. 7c). Thus, while ERH appears dispensable to maintain hESC pluripotency, it is essential to restrict cell identity for proper germ layer differentiation.

ERH represses transposable elements and proximal genes

The activation of pluripotency and alternative-lineage genes after ERH depletion raised the question of where ERH-dependent H3K9me3 acts

Fig. 4 | ERH represses pluripotency and alternative lineage gene activation during hESC differentiation. a Representative images of NANOG (red), SOX17 (red) and DAPI (blue) during 1 day of endoderm differentiation of siControl and siERH H1 hESCs. Scale bars, 50 μm. **b** Representative images of OCT4 (red), PAX6 (green) and DAPI (blue) during 2 days of ectoderm differentiation of siControl and siERH H1 hESCs. Scale bars, 50 μm. **c** Plot of NANOG expression in transcripts per million (TPM) by RNA-seq in siControl and siERH treated H1 hESCs cultured in pluripotency (H1), 1 day endoderm differentiation (DE) and 2 day ectoderm differentiation (EC). Differential expression was assessed by DESeq2, adjusted p-value reported (two-sided Wald test with Benjamini–Hochberg adjustment for multiple comparisons). **d** Plot of KLF5 and ZSCAN4 expression in TPM by RNA-seq in siControl and siERH treated H1 hESCs cultured in pluripotency (H1), 1 day endoderm differentiation (DE) and 2 day ectoderm differentiation (EC). Differential expression was assessed by DESeq2, adjusted p-value reported (two-sided Wald test with Benjamini–Hochberg adjustment for multiple comparisons). **e** GO analysis (PantherDB, statistical overrepresentation) of genes upregulated (padj < =0.05, log2 fold change >= 0.5) in siERH vs siControl H1 hESCs 1 day endoderm differentiation. **f** Radar plot showing cumulative expression profile across indicated human tissues, data downloaded from BBI Descartes database[93], for genes upregulated (padj < =0.05, log2 fold change > = 0.5) in siERH vs siControl H1 hESCs 1 day endoderm differentiation. **g** Radar plot showing cumulative expression profile across indicated human tissues, data downloaded from BBI Descartes database[93], for genes upregulated (padj < = 0.05, log2 fold change >= 0.5) in siERH vs siControl H1 hESCs 2 day ectoderm differentiation. **h** Example early mesodermal genes activated during endoderm differentiation by ERH depletion, TPM values from RNA-seq replicates shown. Differential expression was assessed by DESeq2, adjusted p-value reported (two-sided Wald test with Benjamini–Hochberg adjustment for multiple comparisons). **i** Example late mesodermal genes activated during endoderm differentiation by ERH depletion, TPM values from RNA-seq replicates shown. Differential expression was assessed by DESeq2, adjusted p-value reported (two-sided Wald test with Benjamini–Hochberg adjustment for multiple comparisons). **j** Representative image of DAPI (blue), BRACHYURY (red) of siControl and siERH treated H1 hESCs after 1 day of endoderm differentiation. Scale bars, 50 μm. For all RNA-seq TPM values $n = 3$, except for siCTRL UT where $n = 2$. See also Supplementary Fig. 6 and Supplementary Datas 7,8. Source data are provided as a Source Data file.

during pluripotency exit. During pluripotency-to-endoderm differentiation at protein-coding genes that are upregulated in siERH, H3K9me3 levels only slightly increase in and around those genes (i.e., without siERH) during endoderm differentiation (Supplementary Fig. 8a). By contrast, repeat elements, including L1 LINEs, gained substantial H3K9me3 during endoderm differentiation (Fig. 5a). Because transposable elements are canonical H3K9me3 targets[51] and can function as developmental regulatory elements, including as enhancers for transcription factor binding[31,52–55], we asked whether ERH-dependent TE repression provides a chromatin-level explanation for the gene-expression defects observed during differentiation.

We found that transposable elements were upregulated by ERH knockdown in H1 hESCs, definitive endoderm, and ectoderm, including classes of L1 elements and the hominid-specific[56] SINE VNTR and Alu (SVA) elements (Fig. 5b and Supplementary Fig. 8b, Supplementary Data 9). Satellite repeats were also derepressed (Fig. 5b), as were morula-blastocyst specific *LTR7Ys*[31] and human 8-cell stage expressed *HERVKs*[57] (Fig. 5b and Supplementary Fig. 8c, d), which act as transcription factor binding sites for pluripotency[52,58] and lineage specific genes[55]. After stratifying L1 elements by their evolutionary age[59], we found that ERH preferentially represses evolutionarily young L1 repeats in pluripotent and differentiating hESCs, but broadly represses L1 elements in terminally differentiated fibroblasts (Fig. 5c). By filtering our data for genes expressed during pluripotency that exhibit ERH-dependent repression during differentiation, we uncovered evolutionarily young transposable elements (Fig. 5d and Supplementary Fig. 8e, f) and L1 repeats within 25 kb (Supplementary Fig. 8g) in regions normally marked by H3K9me3 in hESC-derived endoderm (Fig. 5e note different scales on subset to right; Supplementary Fig. 9a).

To assess if repeat expression upon ERH knockdown during endoderm differentiation was due to H3K9me3 loss, we performed H3K9me3 CUT&RUN in siControl and siERH hESCs differentiated to endoderm. We found the increased L1 element RNA expression upon ERH depletion (Fig. 5c) did not globally correspond to a loss of H3K9me3 (Supplementary Fig. 9b). However, when we restricted the analysis to L1 TEs that gained H3K9me3 with at least a 2-fold increase in RNA in siERH endoderm, the L1 loci showed decreased H3K9me3 upon ERH depletion (Fig. 5f). We found repeat element loci with increased RNA expression with (Fig. 5g left) and without H3K9me3 loss (Fig. 5g right) indicating that RNA expression from TEs upon ERH depletion during endoderm differentiation was not necessarily dependent upon H3K9me3 loss. We observe instances of endoderm-specific upregulation of genes proximal to evolutionarily young repeats, such as L1 and LTR7Ys, with reduced H3K9me3 in ERH-depleted endoderm (Supplementary Fig. 9c). ERH therefore represses evolutionarily young and lineage-specific repeats, preventing improper activation of pluripotency and alternative lineage genes during differentiation to maintain lineage specification integrity. The role of H3K9me3 and ERH at this cell fate change likely occurs predominantly at transposable element regions and not gene bodies.

ERH is recruited to chromatin by cell-specific cofactors

Our observation that ERH is required for maintenance of H3K9me3 in fibroblasts (Fig. 1b) but dispensable for hESC H3K9me3 (Fig. 1g) led us to investigate potential ERH protein interactions that may drive the difference in regulatory mechanism. We focus on the pluripotent and terminally differentiated states as they exhibit contrasting requirements for ERH in H3K9me3 maintenance (Fig. 1b–g) and very different H3K9me3 distribution patterns (Fig. 1d, i and Supplementary Fig. Fig. 1g). In *S. pombe* Erh1 is recruited by the RNA-binding factor Mmi1[14]. Mmi1 itself is not seen in mammalian cells[60,61], but since it is a YTH domain-containing RNA-binding factor, we investigated potential interactions of ERH with human YTH domain proteins YTHDC1 and YTHDC2. YTHDC1 regulates H3K9me3 through SETDB1 recruitment and repression of repeat elements in mouse ESCs[62,63], and YTHDC2 has been shown to positively regulate transposable elements and the non-coding RNA LINC-ROR in human hESCs[64]. To specifically interrogate ERH-interacting proteins on chromatin, we isolated soluble nucleoplasm and insoluble chromatin-associated fractions and then performed immunoprecipitation of ERH (Fig. 6a). In fibroblasts but not hESCs, we observed that ERH interacts with YTHDC1 in the chromatin fraction (Fig. 6b,c). ERH did not interact with YTHDC2 in the chromatin fraction in either hESCs or fibroblasts, despite being present in both cell types (Fig. 6b,c). We also probed for SAFB1, a known ERH-interacting protein[65], and observed consistent ERH-SAFB1 interactions in both fibroblasts and pluripotent hESCs (Fig. 6b,c), demonstrating that YTHDC1 but not SAFB1 interactions with ERH are cell type-dependent. To investigate the cause of this differential interaction we first analyzed ERH levels, finding that while ERH RNA is not significantly different between pluripotency and fibroblasts (Fig. 6d) or between pluripotent and differentiated hESCs (Supplementary Fig. 6c), fibroblasts stain more strongly for ERH protein (Fig. 6e). We observe that ERH protein levels are higher in cells on the edge of hESC colonies (Fig. 6f) and become higher in all cells after 1 day of endoderm differentiation (Fig. 6f). These results indicate that ERH involvement in H3K9me3 regulation and RNA-binding protein regulation may be modulated by ERH protein level.

As *S. pombe* Erh1 chromatin recruitment is RNA and Mmi1 dependent, we next tested if chromatin association of ERH was RNA dependent and if either YTHDC1 or YTHDC2 facilitated the recruitment. We employed an immunostaining approach[66] in which permeabilized nuclei were treated with RNase A and then stained for ERH, and found that ERH

https://doi.org/10.1038/s41467-026-76015-3

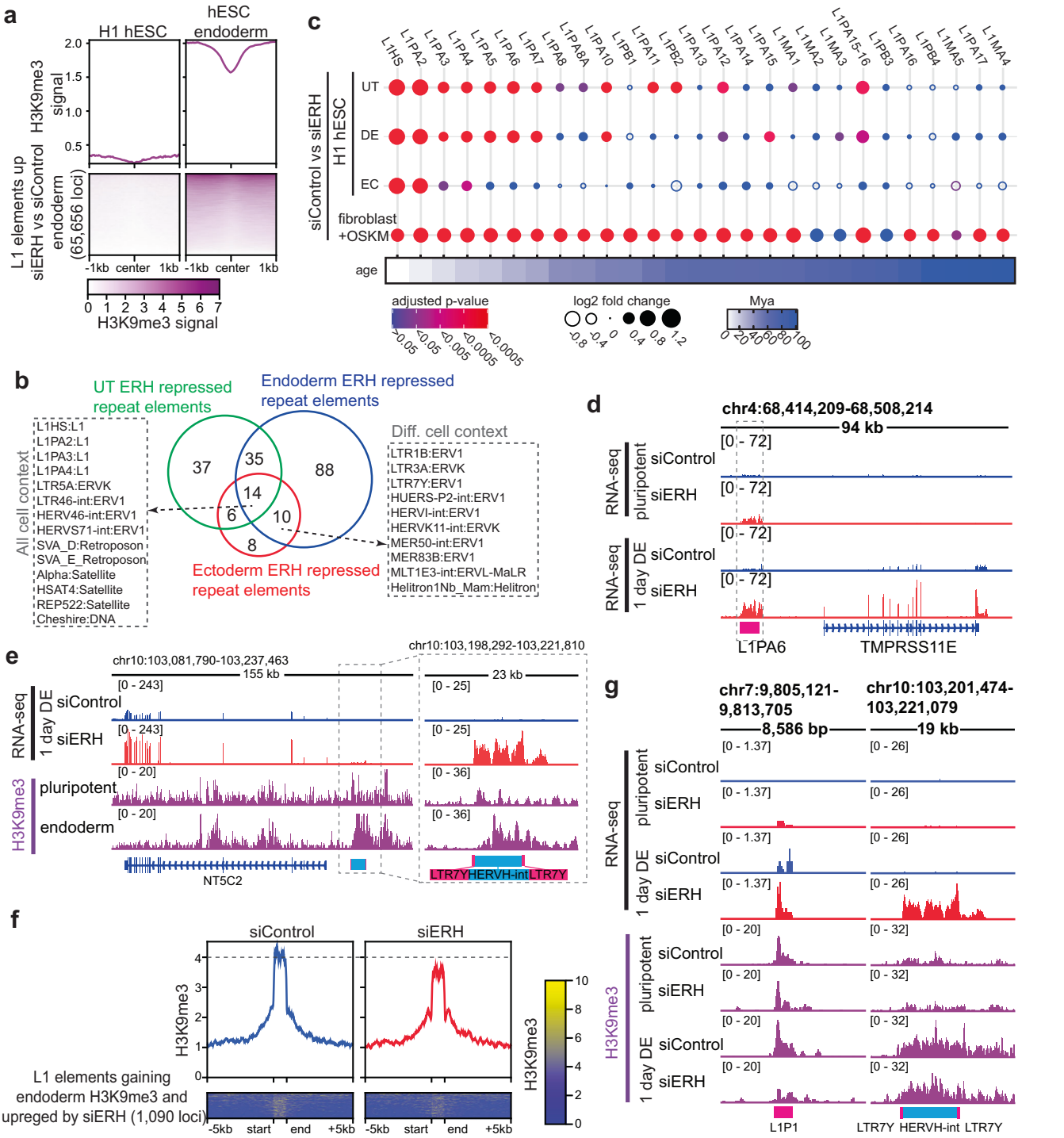

Fig. 5 | ERH represses evolutionarily young transposable elements with regulatory function. a H3K9me3 data from H1 hESCs (GSM1003585) and hESC derived endoderm (GSM916057) at 65,656 L1 element loci +/− 1 kb upregulated (adjusted pvalue < =0.05; log2foldchange > =0.5) by ERH depletion during 1 day endoderm differentiation. **b** Venn diagram showing intersect of repeat classes upregulated (TETranscripts, padj<0.05, log2fc > 0.5) by ERH depletion in H1 hESCs untreated (UT), 1 day endoderm (DE) or 2 day ectoderm (EC) conditions. **c** Expression change and significance, TEtranscripts[89] analysis, of L1 transposable elements in ERH depletion in H1 hESCs untreated (UT), 1 day endoderm (DE) or 2 day ectoderm (EC) listed in order of evolutionary age as determined in ref. 59.Statistical significance for each L1 family was assessed by TEtranscripts/DESeq2 (two-sided Wald test with Benjamini–Hochberg adjustment for multiple comparisons). **d** Example browser track showing expression of L1 element and proximal gene in siControl and siERH treated H1 hESCs in the pluripotent and 1 day DE conditions. **e** Example browser track of gene with promoter proximal repeat element gaining H3K9me3 during endoderm differentiation that is upregulated by ERH depletion. **f** H3K9me3 CUT&RUN signal at L1 elements that exhibited 2-fold RNA increase in siERH vs siControl H1 hESC endoderm and switched from H3K9me3 unmarked in pluripotent to marked in endoderm. **g** Browser track showing RNA-seq of example repeat element and nearby genes in siControl and siERH treated H1 hESCs after 1 day of endoderm differentiation and H3K9me3 tracks from H1 hESCs (GSM1003585) and hESC-derived endoderm (GSM916057). See also Supplementary Figs. 7, 8 and Supplementary Data 10.

https://doi.org/10.1038/s41467-026-76015-3

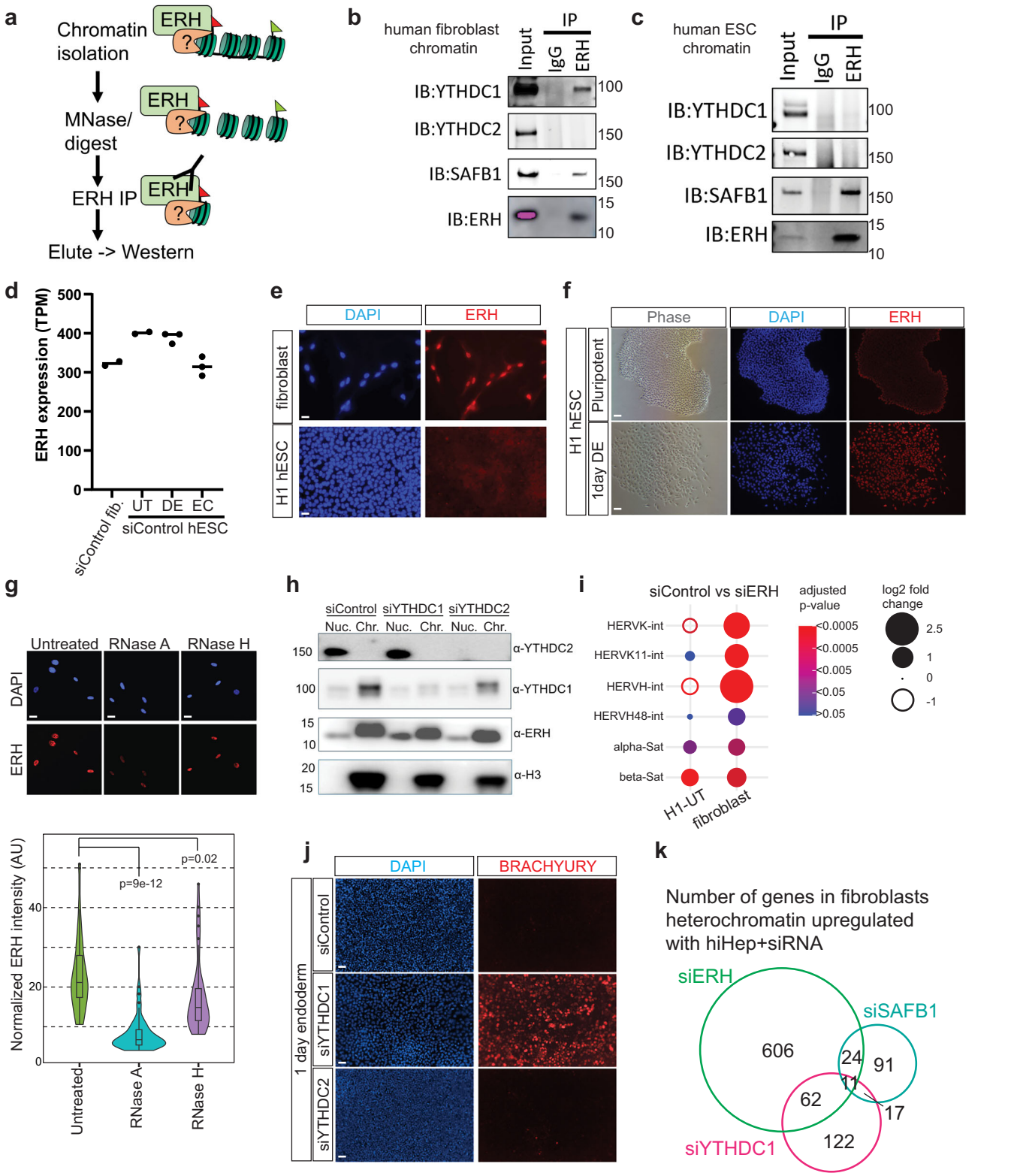

nuclear retention was significantly decreased (Fig. 6g). In contrast, RNase H treatment, which digests DNA:RNA hybrids, did not release ERH from the nucleus (Fig. 6g). In an orthogonal approach, RNase A treatment of fibroblasts during soluble nuclear protein isolation released a portion of chromatin-bound ERH into the nucleoplasm, indicating that its chromatin retention is at least partially RNA-dependent (Supplementary Fig. 10a). To determine if YTHDC1 or YTHDC2 facilitate ERH chromatin recruitment, we targeted each separately with siRNAs in human fibroblasts and observed that YTHDC1 but not YTHDC2 depletion led to decreased levels of ERH in the chromatin fraction and increased ERH in the soluble nuclear fraction (Fig. 6h). We confirmed the role of YTHDC1 in ERH retention utilizing our cell permeabilization and immunostaining assay (Supplementary Fig. 10b). From these experiments we concluded that ERH associates with chromatin with YTHDC1 in fibroblasts, but not in hESCs, and that a subset of ERH protein requires RNA and YTHDC1 for chromatin localization.

Fig. 6 | Cell-type-specific and independent recruitment of ERH to chromatin by RNA-binding proteins regulates gene and repeat repression. a Strategy for identifying chromatin-bound ERH interaction partners by isolation of soluble nucleoplasm and chromatin-associated protein fractions prior to immunoprecipitation. **b** Immunoprecipitation (IP) of ERH from the chromatin fraction of human fibroblasts. Western blot analysis of YTHDC1, YTHDC2, SAFB1, and ERH in the input and IP samples. Images collected from multiple membranes representing same samples loaded at identical concentrations. **c** Immunoprecipitation (IP) of ERH from the chromatin fraction of human ESCs. Western blot analysis of YTHDC1, YTHDC2, SAFB1, and ERH in the input and IP samples. Images collected from multiple membranes representing same samples loaded at identical concentrations. **d** ERH expression (TPM) from RNA-seq in siControl treated human fibroblasts, pluripotent hESCs, 1 day endoderm differentiated hESCs (DE), and 2 day ectoderm differentiated hESCs (EC). (n = 2 for siControl fibroblasts and UT H1 hESCs, $n = 3$ for siControl DE and EC H1 hESCs). **e** ERH staining in human fibroblasts and pluripotent H1 hESCs, DAPI (blue), ERH (red). Scale bars, 20 μm. Staining and imaging performed in parallel using same conditions and microscope settings for both samples. **f** ERH staining in pluripotent H1 hESCs and 1 day endoderm differentiated H1 hESCs, DAPI (blue), ERH (red). Scale bars, 50 μm. Staining and imaging performed in parallel using same conditions and microscope settings for both samples. **g** Immunofluorescence (IF) of ERH after RNase A and RNase H treatment. Quantification of nuclear ERH mean fluorescence intensity is shown as box plots ($n = 39$, 46, and 38, nuclei per untreated, RNAse A, and RNAse H condition; center line, median; box, 25–75th percentile (IQR); whiskers, 1.5 x IQR; violin plot represents the minima/maxima of the data. Statistical significance was assessed using a two-sided Mann-Whitney U test versus untreated control. Scale bars, 20 μm. **h** Western blot of ERH, YTHDC1, and YTHDC2 in nucleoplasm (nuc.) and chromatin-associated (chr.) protein fractions of human fibroblasts after siYTHDC1 and siYTHDC2 treatment. $N = 2$ biological replicates. **i** Expression change and significance, TEtranscripts[89] analysis, of HERVK HERVH and satellite repeats in hESCs and human fibroblasts after siERH. Differential expression was assessed with DESeq2 (two-sided Wald test with Benjamini–Hochberg adjustment for multiple comparisons). Repeats with adjusted p-value < 0.05 and log2 fold change > 0.5 were called as significantly upregulated. **j** Immunofluorescence (IF) of BRACHYURY in siCTRL, siYTHDC1 and siYTHDC2 after 1 day endoderm differentiation. Scale bars, 50 μm. Staining and imaging performed in parallel using same conditions and microscope settings for all samples. **k** Venn diagram of gene co-regulation after siERH, siYTHDC1 and siSAFB1 in human fibroblasts after addition of hepatic reprogramming factors, FOXA3, HNF1A, HNF4A. All IP WB and immunofluorescence experiments presented in this figure were repeated independently with similar results at least $N = 2$ times. See also Supplementary Fig. 9. Source data are provided as a Source Data file.

We next assessed for co-regulation of common targets by ERH, YTHDC1, and YTHDC2, first by evaluating expression changes of published YTHDC1 and YTHDC2 targets, ERVK elements repressed by YTHDC1[67], and HERVH elements activated by YTHDC2[64]. ERH represses HERVK and HERVH elements in fibroblasts treated with OSKM factors but not in pluripotent hESCs (Fig. 6i), matching the interaction pattern of ERH with YTHDC1 (Fig. 6b, c). Major satellite repeats, which are regulated by SAFB1[68], are repressed by ERH in both fibroblasts and pluripotent hESCs (Fig. 6i).

As we found that ERH interacts with YTHDC1 in differentiated cells but not pluripotent cells, we investigated if YTHDC1 depletion recapitulates aspects of ERH depletion during hESC differentiation. Depletion of YTHDC1 but not YTHDC2 during endoderm differentiation of hESCs resulted in an increase of BRACHYURY staining, indicative of a mesodermal fate (Fig. 6j), matching our findings from ERH depletion during endoderm differentiation (Fig. 4j). We found that ERH represses many genes not regulated by its interacting partners YTHDC1 and SAFB1, which predominantly repress different subsets of ERH targets (Fig. 6k). Taken together, the results indicate that various RNA-binding proteins function non-redundantly to recruit ERH to different targets. Based upon these findings, we propose that ERH interacts with RNA-binding proteins, including YTHDC1 and SAFB1, to facilitate cell-specific repression of genes and repeat elements (Fig. 6i).

Discussion

We discovered that depletion of ERH reverts the H3K9me3 landscape in terminally differentiated cells to an hESC-like state, permissive to activation of early embryonic genes. This surprising result led us to investigate the role of ERH in establishing gene repression during the earliest stages of mammalian lineage segregation, in maintaining repression of pluripotency, and enabling germ layer specification. We found that ERH controls H3K9me3 for repression of naïve and alternative lineage genes during the cell fate commitment of totipotent cells to ICM and trophectoderm in mouse blastocysts, as well as of hESCs to the endoderm and ectoderm cell lineages, to enforce cell fate and prevent anomalous gene activation. Between the three systems we employed, mouse preimplantation development, hESC differentiation, and fibroblast iPSC reprogramming, we observe that ERH commonly repressed a shared set of naïve genes, such as *ZSCAN4*, across all systems, indicating that ERH is involved in both the initial repression of this early transcriptional program and in maintaining repression in terminally differentiated cells. Remarkably, Erh1 is the sole apparent mechanism for repressing meiotic genes in *S. pombe*, is conserved in repressing germ cell genes in mammals[16], and has expanded to fundamentally control diverse other types of developmental genes and stages.

In a developmental context, the failure to repress 2-cell, 8-cell, and pluripotency genes after ERH knockdown results in delays in the expression of specific lineage genes, including primitive endoderm genes in mouse blastocysts and various endoderm and ectoderm genes during hESC differentiation. Furthermore, we demonstrated that ERH is necessary to maintain repression of alternative lineage genes, as ERH depletion elicited precocious expression of genes typical of later cell differentiation in mouse blastocysts and human hESCs, as well as heterochromatinized genes during initial iPSC reprogramming. We observed that evolutionarily young transposable elements, including the human-specific *LTR7Ys*[31], are especially upregulated by ERH depletion during hESC differentiation and iPSC reprogramming. Much of the lineage-specific expression changes upon ERH depletion during hESC differentiation may be attributed to increased accessibility of transcription factor binding sites among derepressed repeats[31,52,55].

A key finding is that ERH depletion in human fibroblasts reverted the H3K9me3 chromatin landscape to a hESC-like state. The reversion to a hESC-like H3K9me3 landscape permits binding of SOX2 in fibroblasts to endogenous hESC SOX2 targets, activating embryonic genes. That ERH is necessary for maintaining the broad H3K9me3 domains observed in somatic cells, but is dispensable for maintaining hESC H3K9me3 peaks, is consistent with our observation that ERH depletion in hESCs did not change global H3K9me3 levels. We suggest that the residual H3K9me3 peaks in pluripotent cells, enriched for zinc-finger motifs and KAP1 binding, may be H3K9me3 nucleation sites and that, during differentiation, ERH is essential for the spread of H3K9me3 from these sites. Importantly, when ERH is knocked down in fibroblasts, we observe increased activation of many genes and transposable elements that harbor a residual H3K9me3 peak, yet lose broad H3K9me3, indicating that residual H3K9me3 peaks are not sufficient to block gene activation. Our knowledge of H3K9 methylation nucleation and spread has been primarily elucidated through studies in *S. pombe*[69–71], leaving further investigation needed into how H3K9me3 nucleation and spread occur in multicellular organisms.

We identify that ERH interacts with and is partially recruited to the chromatin by the RNA-binding protein YTHDC1 in somatic cells, but not in pluripotent hESCs. We find that ERH and YTHDC1 repress similar targets in fibroblasts and differentiating hESCs, but not in homeostatic pluripotent hESCs. In contrast, we observe that ERH interacts with the

RNA-binding protein SAFB1 in both hESCs and human fibroblasts, and likewise, both repress satellite repeat expression in hESCs and fibroblasts. Differentiation state-dependent changes in ERH-interacting partners may be driven by lower levels of ERH protein, which we show is regulated at the protein level in pluripotent cells compared to differentiated cells. The mechanism regulating ERH protein stability requires further investigation, but it is notable that ERH is ubiquitinated at lysine 41 in multiple studies[72]. The function of this modification in ERH stability and how it may be regulated in a differentiation-specific manner will be a point for future studies. Our knockdowns of YTHDC1 and gene expression analysis of YTHDC1 and SAFB1 fail to fully explain how ERH is recruited to chromatin to repress transcription. We thus speculate that ERH is recruited to cell-type-specific genes and repeats through a diverse network of chromatin-associated RNA-binding factors that are yet to be fully identified.

We observe in mouse development and hESC systems that ERH is functionally required in multiple developmental contexts to repress meiotic and gametogenic genes, as it is in *S. pombe*[14], although the gene members targeted by ERH have greatly evolved and expanded in mammals. Our findings on meiotic gene repression are supported by the recent identification of ERH in a screen for proteins silencing germline genes in mESCs[73]. Other aspects of Erh1 function in *S. pombe*, such as the targeting of RNAs for degradation by the RNA exosome[14], appear to be conserved as we observed upregulation of developmental genes typically downregulated by RNA exosome degradation[74]. ERH was recently found by mass spectrometry to associate with the Microprocessor and NEXT complexes in mouse ESCs[75]. Evolutionarily divergent functions of ERH may be driven by evolutionarily young transposable elements that retain RNA expression, similar to how transposable elements have influenced the evolution of KRAB Zinc finger proteins' DNA-dependent targeting of H3K9me3[76,77].

We found that ERH mediates gene repression at the earliest stages of development and is essential for maintaining this repression in terminally differentiated cells. Our findings advance the understanding of how heterochromatin-based repression is established and maintained during mammalian development. We propose that understanding the mechanisms by which ERH is employed to direct H3K9me3 to specific loci in a developmentally coordinated fashion will be crucial to modulating developmental H3K9me3 rearrangements to achieve greater control of cell identity.

Methods

Cell lines culture and condition

Human H1 ES cells were obtained from WiCell (WA01), grown on Matrigel coated wells and cultured in mTeSR1 (Stem Cell Tech, 85850) medium at 37 °C and 5% CO_2. Medium was changed daily. Human BJ foreskin fibroblasts were obtained from ATCC (CRL-2522) and cultured in Eagle's Minimum Essential Medium (EMEM, Sigma-Aldrich M2279) supplemented with 10% fetal bovine serum (FBS, Hyclone SH30071) and 2 mM Glutamax (ThermoFisher 35050061) at 37 °C and 5% CO_2.

Mouse embryo work

Mouse embryo experimentation was approved by the Biological Resource Center Institutional Animal Care and Use Committee (IACUC), Agency for Science, Technology and Research (IACUC Protocol 806983). C57BL/6 wild-type 3–4-week-old female mice were superovulated using 5 IU of pregnant mare serum (PMS, National Hormone and Peptide Program) gonadotropin given intraperitoneally and 5 IU of recombinant chorionic gonadotrophin (CG, National Hormone and Peptide Program) given 48 h after and immediately before mating, according to animal ethics guidelines of the University of Pennsylvania. Embryos were flushed from oviducts of plugged females using M2 medium (Merck) and cultured in KSOM + AA (Merck) covered by mineral oil (Sigma, M-5310), at 37 °C and 5% CO2.

Mouse embryo immunofluorescence and microscopy

Embryos were fixed in 4% paraformaldehyde (Electron Microscopy Sciences, 15710) for 30 min at room temperature washed twice in PBS with 0.1% Triton X-100 (Millipore Sigma, T8787), permeabilized for 20 min in PBS with 0.5% Triton X-100, and blocked in 3% bovine serum albumin (Gemini Bio, 700-100 P) for 30 min. Embryos were then incubated at 4 °C overnight in primary antibodies diluted in blocking solution at the following concentrations: ERH (Abcam, ab166620) at 1:200, Keratin-8 (DSHB, THROMA-I) at 1:20, H3K9me3 (Abcam, ab8898) at 1:1000, and CDX2 (Invitrogen, ZC007) at 1:200. After primary antibody incubation, embryos were washed five times for 20 min in PBS with 0.1% Triton X-100 and incubated for 30 min in Alexa Fluor-conjugated secondary antibodies (Invitrogen, A32731, A32723, A32733, A32728 and A11006) diluted in blocking solution to 1:500. Phalloidin-Alexa Fluor 555 (Invitrogen, A34055) diluted to 1:500 and DAPI (Sigma, 10236276001) diluted to 1:500 in blocking solution were also used to label F-actin and DNA, respectively. Embryos were washed three times in PBS with 0.1% Triton X-100 before mounting in PBS covered with mineral oil in an 8-well µ-Slide (Ibidi, #80827). Embryos were imaged using a laser-scanning confocal microscope (Leica SP8) with a water-immersion Apochromat 40× 1.1 NA objective and HyD detectors. Samples were excited with standard laser lines (405-nm, 488-nm, 552-nm, 638-nm).

Mouse embryo siRNA injection experiments

Microinjections were performed using a FemtoJet (Eppendorf). For ERH knockdown experiments, mouse embryos were injected with two siRNAs (Qiagen, S104403294 & S104403287) against ERH at a total concentration of 400 nM. For knockdown experiments AllStars negative control siRNA (Qiagen, 1027281) was injected in embryos at a concentration of 400 nM.

Differentiation of hESCs

Prior to differentiation, for samples to be analyzed by RNA-seq, cells grown to a density of 80% were digested with Accutase (Stem Cell Technologies, 07920) for 7 min. Then, DMEM/F12 was added and gently pipetted to generate a cell suspension. After centrifugation, cells were resuspended in mTeSR1 medium with 5uM ROCK inhibitor Y-27632 (Cayman Chemical, 10005583) and seeded at 8×10^5–1×10^6 cells per well in a 6 well plate coated with Matrigel (Millipore Sigma, CLS354277) 24 h prior to differentiation treatment. For definitive endoderm differentiation of hESCs, mTeSR1 medium was removed and cells were cultured in DMEM/F12 (Thermo Fisher, 11320033) supplemented with 10% (v/v) Fetal Bovine Serum (Hyclone, SH30071) with 100 ng/ml Activin A (Peprotech, 120-14 P) and 3uM CHIR99021 (Cayman Chemical, 13122). For ectoderm differentiation of hESCs, mTeSR medium was removed and cells were cultured in DMEM/F12 with 5uM Retinoic Acid (Cayman Chemical, 11017).

Cell culture siRNA transfection experiments

All ERH knockdown experiments were performed with two cycles of siRNA transfection (Silencer Select siRNA, Thermo Fisher, s4815), three days apart. Transfections were performed in fibroblasts using 5 nM final concentration of siRNA and in hESCs using a 10 nM final concentration of siRNA and 2.5ul/ml final concentration of Lipofectamine RNAiMAX (Thermo Fisher #31985070).

Reprogramming factor expression experiments

We utilized the CytoTune-iPS 2.0 Sendai reprogramming kit (ThermoFisher, A16517) to express Oct4, SOX2, KLF4 and cMyc in BJ fibroblasts. Cells were treated according to the manufacturer's instructions three days after the second of two cycles of siRNA transfection.

Cell culture immunofluorescence and microscopy

For immunofluorescence of human fibroblasts and hESCs cells were washed briefly with PBS, and fixed in 4% paraformaldehyde in PBS for

10 min. Fixed cells were washed 3 times with PBS, permeabilized with ice-cold 0.1% Triton-X in PBS for 10 min, and washed twice with PBS-T (PBS, 0.05% Tween-20). Samples were blocked with 3% donkey serum (Millipore Sigma, D9663) in PBS for 2 h at room temperature and incubated overnight at 4 °C using the following concentrations: anti-H3K9me3 (1:300, Abcam ab8898), anti-H3K27me3 (1:300, Active Motif, 39155), anti-SOX2 (1:200, Cell Signaling, 23064), anti-OCT4 (1:200, Abcam, ab19857), anti-PAX6 (1:200, BD Biosciences, 561462), anti-BRACHYURY (1:200, Cell Signaling, 81694) in 3% donkey serum in PBS. Cells were washed three times with PBS-T and then incubated with AlexaFluor 488- or 594-conjugated secondary antibodies raised in donkey (Thermo Fisher, See Methods) at a 1:500 dilution in 3% donkey serum in PBS.

Total RNA isolation and sequencing

BJ fibroblasts grown in a 6-well dish were washed twice with cold PBS, followed by addition of 1 mL TRIzol reagent (ThermoFisher 15596026) and transferred to a chilled 1.5 mL tube using a cell scraper. The cells were homogenized by pipetting through a 25 G needle attached to a 2 mL syringe ten times. 200 μl of chloroform was added to the cells and vortexed for 15 s, followed by a room temperature incubation of 3 min. Phase separation of nucleic acids and protein was performed by centrifugation at 12,000 x g for 15 min at 4 °C. The upper aqueous phase containing RNA was then transferred to a fresh chilled tube. RNA was precipitated from the aqueous phase by adding an equal volume of isopropyl alcohol, followed by a 10 min incubation at room temperature. The RNA was pelleted by centrifugation at 12,000 x g for 10 min at 4 °C. After removal of supernatant, the pellet was washed twice with 1 mL 75% ethanol, and resuspended in nuclease-free water. RNA quality was verified using a high-sensitivity RNA screentape (Agilent 5067-5576). 1ug of total RNA was sent to Novogene, who assembled and sequenced bulk RNA-seq libraries. Two to three biological replicates were prepared for each condition.

Immunoprecipitation and Western blotting

Chromatin fractions for immunoprecipitation were prepared using the Subcellular Protein Fractionation Kit for Cultured Cells (ThermoFisher 78840) and performed following the manufacturer's protocol. Immunoprecipitation was performed from the resulting chromatin fraction as follows. An aliquot of chromatin was reserved as the input sample. Protein G Dynabeads (ThermoFisher 10003D) were first washed twice with 500ul PBS-T then resuspened in 100ul PBS equal to 4X the original slurry volume. 5 μg of anti-ERH antibody (abcam 166620) was conjugated to Dynabeads in low protein binding tubes (Eppendorf 022431081) by incubating on a rotating rack at 4 °C for 4 h. Antibody-conjugated beads were washed twice with 500ul PBS-T, blocked with 1% Donkey serum in PBS for 1 hour, washed 2 times with 500ul PBST, then resuspended in 50 μl PBS. 50ul of chromatin fraction was added to the resuspended antibody-conjugated beads and incubated at 4 °C overnight. After incubation the beads were washed five times with 500ul PBS-T and eluted in SDS loading dye for 8 min at 90 °C. Protein samples were mixed with 5X SDS-Gel Loading Buffer (250 mM Tris pH 6.8, 10% SDS, 0.5% Bromophenol Blue, 50% Glycerol, 5% β-Mercaptoethanol) and were denatured at 90°C for 5 min. Samples were loaded in BioRad Mini-PROTEAN 4-20% TGX Precast Protein Gels (BioRad 4568091) and run using BioRad running buffer (BioRad 1610732). Wet transfer to 0.2 μm PVDF membrane (BioRad 1620177) was performed using BioRad transfer buffer (BioRad 1610734) containing 20% methanol. Membranes were blocked overnight in 5% nonfat dairy milk in TBS-T at the following concentrations: anti-ERH (1:500, Sigma-Aldrich, HPA002567), anti-YTHDC1 (1:500, Cell Signaling, 81504 s), anti-YTHDC2 (1:1,000, abcam, ab220160), anti-SAFB1 (1:500, Proteintech, 21857-1-AP) in 3% milk/TBS-T. Fluorescent antibodies (BioRad 12004162) were diluted 1:5,000 in 3% milk/TBS-T. Blots were imaged using a BioRad ChemiDoc MP imaging system. Uncropped images of all blots presented in figures are provided in Source Data.

CUT&RUN experiments

CUT&RUN was performed as described in ref. 78, with digitonin and NaCl in wash buffers optimized for permeabilization of BJ fibroblasts and retainment of SOX2 on chromatin as performed in ref. 79. Next, BJ fibroblasts were detached from cell culture plates with Accutase (STEMCELL Technologies 07920), washed, bound to magnetic concanavalin A beads, and permeabilized with a dig-wash buffer (0.1% digitonin, 20 mM HEPES pH 7.5, 75 mM NaCl, 0.5 mM Spermidine, EDTA-free protease inhibitor). Bead-bound cells were incubated with a SOX2 (CST, clone D9B8N, 23064, 1:100) or H3K9me3 antibody (abcam ab8898, 1:100) at 4 °C overnight. The following morning, the cells were washed twice with dig-wash buffer, incubated with pA/G-MNase for an hour at 4 °C, and washed twice more. After chilling cells on an ice block for 5 min, MNase was activated for 30 min by addition of 2 mM $CaCl_2$. The reaction was stopped by adding an equal volume of 2X STOP buffer (340 mM NaCl, 20 mM EDTA, 4 mM EGTA, 0.05 mg/mL glycogen, 50 ug/mL RNase A). Digested chromatin was extracted from permeabilized cells at 37 °C for 30 min, and DNA was purified by phenol-chloroform. Libraries were prepared as previously described[80]. Two to three biological replicates were prepared for each condition.

CUT&RUN data processing

Paired-end CUT&RUN reads were mapped to the human genome build hg38 using bowtie2[81] (v2.3.4.1) with run parameters --local --very-sensitive --no-unal --no-mixed --no-discordant -I 10 -X 1000. A quality-filtered BAM file was generated with the command samtools (v1.16.1) view -q 5 -f 2 -bS. Global scaling factors (SF) for siERH and siControl H3K9me3 data sets were calculated using the default parameters of ChIPSeqSpikeInFree[82] (R v3.6.3). Bigwig files for visualization were generated from indexed BAM files with command bamCoverage --smoothLength 10 --normalizeUsing CPM --scaleFactor 1/SF --ignoreForNormalization chrM (deeptools 3.5.0). BED files were generated from BAMs using the bedtools command bamToBed (bedtools v2.27.1). BED files were converted to bedgraph format using the bedtools command genomecov. Peaks were called on the bedgraph files with SEACR[83] (v1.3), using the stringent setting and selecting the top 0.01% of regions by AUC. Peak lists for downstream analyzes were derived from individual replicates or the union of overlapping sites from biological triplicates, as indicated in the text and figures. Enrichment analysis of known DNA binding motifs was performed using HOMER[84].

CUT&RUN footprinting was performed using SOX2 CUT&RUN at SOX2 peaks gained upon ERH knockdown. Motif instances of KLF4 (HOMER motif 192) and OCT4 (HOMER motif 254) within these regions were identified. By using CENTIPEDE, CUT&RUN fragment cut points were plotted relative to the KLF4 or OCT4 motif center across a 50 bp window. Motif-centered cleavage profiles were generated by averaging cut point fractions across all motif instances. Comparisons between siCTRL and siERH conditions were used to assess relative changes in motif-centered protection patterns consistent with altered transcription factor engagement.

Heatmaps

Heatmaps were generated with deeptools[85] version 3.5.0. Counts matrices were generated with command computeMatrix reference-point --missingDataAsZero --referencePoint center. Figures were produced with the plotHeatmap command.

Correlation plots

To assess genome wide similarity between hBJ siERH H3K9me3, hBJ siControl H3K9me3, and H1-hESC H3K9me3 data sets, the Pearson correlation of peak overlap was calculated using the Intervene tool[86]. In

brief, peak files for individual H3K9me3 replicates were processed with the command intervene pairwise --I *H3K9me3.bed --compute fract --htype color. Visualization of Pearson correlation of fractional overlap between peak sets were generated on https://intervene.shinyapps.io/intervene.

RNA-seq data analysis

RNA-seq reads (paired-end) were mapped to the mm10 or hg38 genome for mouse and human experiments respectively using STAR[87] (2.7.10b). The mapped reads to genes were counted using featureCounts[88]. For counting repeat mapping reads the TE count function from TEtranscripts[89] was run on STAR-aligned bam files using the hg38 repeatmasker gtf file annotation. The output count files were analyzed by DESeq2[90] to detect differentially expressed genes (Benjamini adjusted p-value < 0.05, log2 fold change > 1 or log2 fold change > 1.5). Genes and repeats with fewer than ten total mapped reads were excluded from DESeq2 and TETranscripts analysis. TPM, FPKM and RPM were calculated using an in-house R script.

Mouse blastocyst image analysis

3D visualizations and analysis of embryos were performed using Imaris 8.2 or Imaris 9.7 software (Bitplane). The manual surface rendering module was used for cellular and nuclear segmentation, using phalloidin and DAPI signals to define cellular and nuclear boundaries, respectively. Quantifications of immunofluorescence intensity were performed by measuring the mean fluorescence intensity of voxels within the segmented object, standardized DAPI to account for light scattering.

Cell culture image analysis

Quantification of nuclear area and signal intensity was performed using the Nuclear Morphometric Analysis (NMA) plugin for ImageJ[91]. In ImageJ saturated pixels was set to 0.35% prior to processing. NMA plugin was run using the following settings: show ellipse and use watershed options selected, minimum nuclei area = 150, maximum nuclei area = 6000, nuclei intensity segmentation threshold = 95, nuclei insertion intensity = 93%.

Gene ontology enrichment analysis

Gene ontology enrichment analysis was performed using PANTHER[92] (v18.0) with settings, statistical overrepresentation test: GO biological process complete, all genes in the database were used as the background reference list, and statistical significance was determined using Fisher's Exact test with false discovery rate.

Statistical analysis

Statistical analyzes were performed in GraphPad Prism, the R software for statistical computing and with DESeq2. Pairwise comparisons were analyzed using an unpaired, two-tailed Student's t-test. Correlation was analyzed with a two-tailed Pearson's Correlation test. Significant overlap between gene sets was analyzed with the hypergeometric test. Differential gene expression analysis was performed using DESeq2, which calculates p-values by the Wald test and adjusted p-values corrected for multiple testing using the Benjamini and Hochberg method. Reproducibility was confirmed by independent experiments.

Ethics statement

Human embryonic stem cell H1 was purchased from WiCell Research Institute (WiCell).

Reporting summary

Further information on research design is available in the Nature Portfolio Reporting Summary linked to this article.

Data availability

Source data are provided with this paper. RNA-seq and CUT&RUN datasets generated in this study have been deposited in the NCBI Gene Expression Omnibus and are available under the following accession codes: GSE268901 (RNA-seq datasets generated in this study); GSE268961 (CUT&RUN datasets generated in this study). Previously published datasets used in this study are available under the following accession codes: GSM1003585 (H1 hESC H3K9me3); GSE123229 (H1 hESC HP1α); GSM1701825 (H1 hESC HP1α); GSM916057 (hESC-derived CD184+ endoderm H3K9me3); GSE44183 (human 8-cell embryo RNA-seq) Source data are provided with this paper.

References

1. Nicetto, D. et al. H3K9me3-heterochromatin loss at protein-coding genes enables developmental lineage specification. *Science* **363**, 294–297 (2019).
2. Bilodeau, S., Kagey, M. H., Frampton, G. M., Rahl, P. B. & Young, R. A. SetDB1 contributes to repression of genes encoding developmental regulators and maintenance of ES cell state. *Genes Dev.* **23**, 2484–2489 (2009).
3. Becker, J. S. et al. Genomic and proteomic resolution of heterochromatin and its restriction of alternate fate genes. *Mol. Cell* **68**, 1023–1037.e15 (2017).
4. Xu, R. et al. Stage-specific H3K9me3 occupancy ensures retrotransposon silencing in human pre-implantation embryos. *Cell Stem Cell* **29**, 1051–1066.e8 (2022).
5. Zhang, J. et al. Distinct H3K9me3 heterochromatin maintenance dynamics govern different gene programmes and repeats in pluripotent cells. *Nat. Cell Biol.* **26**, 2115–2128 (2024).
6. Schulz, K. N. & Harrison, M. M. Mechanisms regulating zygotic genome activation. *Nat. Rev. Genet* **20**, 221–234 (2019).
7. Xu, R. et al. Unreprogrammed H3K9me3 prevents minor zygotic genome activation and lineage commitment in SCNT embryos. *Nat. Commun.* **14**, 4807 (2023).
8. Sankar, A. et al. KDM4A regulates the maternal-to-zygotic transition by protecting broad H3K4me3 domains from H3K9me3 invasion in oocytes. *Nat. Cell Biol.* **22**, 380–388 (2020).
9. Wang, C. et al. Reprogramming of H3K9me3-dependent heterochromatin during mammalian embryo development. *Nat. cell Biol.* **20**, 620–631 (2018).
10. Yu, H. et al. Dynamic reprogramming of H3K9me3 at hominoid-specific retrotransposons during human preimplantation development. *Cell Stem Cell* **29**, 1031–1050.e12 (2022).
11. Burton, A. et al. Heterochromatin establishment during early mammalian development is regulated by pericentromeric RNA and characterized by non-repressive H3K9me3. *Nat. Cell Biol.* **22**, 767–778 (2020).
12. Bhanu, N. V., Sidoli, S. & Garcia, B. A. Histone modification profiling reveals differential signatures associated with human embryonic stem cell self-renewal and differentiation. *Proteomics* **16**, 448–458 (2016).
13. Ugarte, F. et al. Progressive chromatin condensation and H3K9 methylation regulate the differentiation of embryonic and hematopoietic stem cells. *Stem Cell Rep.* **5**, 728–740 (2015).
14. Sugiyama, T. et al. Enhancer of rudimentary cooperates with conserved RNA-processing factors to promote meiotic mRNA decay and facultative heterochromatin assembly. *Mol. Cell* **61**, 747–759 (2016).
15. Xie, G. et al. A conserved dimer interface connects ERH and YTH family proteins to promote gene silencing. *Nat. Commun.* **10**, 251 (2019).
16. McCarthy, R. L. et al. Diverse heterochromatin-associated proteins repress distinct classes of genes and repetitive elements. *Nat. Cell Biol.* **23**, 905–914 (2021).

17. Kuznetsov, D. et al. OrthoDB v11: annotation of orthologs in the widest sampling of organismal diversity. *Nucleic Acids Res.* **51**, D445–D451 (2023).
18. Stephens, A. D. et al. Chromatin histone modifications and rigidity affect nuclear morphology independent of lamins. *Mol. Biol. Cell* **29**, 220–233 (2018).
19. Stoll, G. A., Pandiloski, N., Douse, C. H. & Modis, Y. Structure and functional mapping of the KRAB-KAP1 repressor complex. *EMBO J.* **41**, e111179 (2022).
20. Soufi, A., Donahue, G. & Zaret, K. S. Facilitators and impediments of the pluripotency reprogramming factors' initial engagement with the genome. *Cell* **151**, 994–1004 (2012).
21. Taing, L. et al. Cistrome Data Browser: integrated search, analysis and visualization of chromatin data. *Nucleic Acids Res.* **52**, D61–D66 (2024).
22. Zheng, R. et al. Cistrome Data Browser: expanded datasets and new tools for gene regulatory analysis. *Nucleic Acids Res.* **47**, D729–D735 (2019).
23. Yu, X. et al. Recapitulating early human development with 8C-like cells. *Cell Rep.* **39**, 110994 (2022).
24. Zou, Z. et al. Translatome and transcriptome co-profiling reveals a role of TPRXs in human zygotic genome activation. *Science* **378**, abo7923 (2022).
25. Taubenschmid-Stowers, J. et al. 8C-like cells capture the human zygotic genome activation program in vitro. *Cell Stem Cell* **29**, 449–459.e6 (2022).
26. Cacchiarelli, D. et al. Integrative analyses of human reprogramming reveal dynamic nature of induced pluripotency. *Cell* **162**, 412–424 (2015).
27. Bi, Y. et al. Cell fate roadmap of human primed-to-naive transition reveals preimplantation cell lineage signatures. *Nat. Commun.* **13**, 3147 (2022).
28. Xue, Z. et al. Genetic programs in human and mouse early embryos revealed by single-cell RNA sequencing. *Nature* **500**, 593–597 (2013).
29. Wang, J. et al. Primate-specific endogenous retrovirus-driven transcription defines naive-like stem cells. *Nature* **516**, 405–409 (2014).
30. Lu, X. et al. The retrovirus HERVH is a long noncoding RNA required for human embryonic stem cell identity. *Nat. Struct. Mol. Biol.* **21**, 423–425 (2014).
31. Ai, Z. et al. Krüppel-like factor 5 rewires NANOG regulatory network to activate human naive pluripotency specific LTR7Ys and promote naive pluripotency. *Cell Rep.* **40**, 111240 (2022).
32. Gadepalli, V. S., Kim, H., Liu, Y., Han, T. & Cheng, L. XDeathDB: a visualization platform for cell death molecular interactions. *Cell Death Dis.* **12**, 1156 (2021).
33. Gao, Y. et al. Protein expression landscape of mouse embryos during pre-implantation development. *Cell Rep.* **21**, 3957–3969 (2017).
34. Ralston, A. & Rossant, J. Cdx2 acts downstream of cell polarization to cell-autonomously promote trophectoderm fate in the early mouse embryo. *Dev. Biol.* **313**, 614–629 (2008).
35. Lim, H. Y. G. et al. Keratins are asymmetrically inherited fate determinants in the mammalian embryo. *Nature* **585**, 404–409 (2020).
36. Domingo-Muelas, A. et al. Human embryo live imaging reveals nuclear DNA shedding during blastocyst expansion and biopsy. *Cell* **186**, 3166–3181.e18 (2023).
37. Falco, G. et al. Zscan4: a novel gene expressed exclusively in late 2-cell embryos and embryonic stem cells. *Dev. Biol.* **307**, 539–550 (2007).
38. Hamatani, T., Carter, M. G., Sharov, A. A. & Ko, M. S. H. Dynamics of global gene expression changes during mouse preimplantation development. *Dev. Cell* **6**, 117–131 (2004).
39. Boussicault, L. et al. CYP46A1, the rate-limiting enzyme for cholesterol degradation, is neuroprotective in Huntington's disease. *Brain* **139**, 953–970 (2016).
40. Chalhoub, G. et al. Carboxylesterase 2 proteins are efficient diglyceride and monoglyceride lipases possibly implicated in metabolic disease. *J. Lipid Res* **62**, 100075 (2021).
41. Artus, J., Piliszek, A. & Hadjantonakis, A.-K. The primitive endoderm lineage of the mouse blastocyst: sequential transcription factor activation and regulation of differentiation by Sox17. *Dev. Biol.* **350**, 393–404 (2011).
42. Teo, A. K. K., Valdez, I. A., Dirice, E. & Kulkarni, R. N. Comparable generation of activin-induced definitive endoderm via additive Wnt or BMP signaling in absence of serum. *Stem Cell Rep.* **3**, 5–14 (2014).
43. Messmer, T. et al. Transcriptional heterogeneity in naive and primed human pluripotent stem cells at single-cell resolution. *Cell Rep.* **26**, 815–824.e4 (2019).
44. Dubois, A. et al. H3K9 tri-methylation at Nanog times differentiation commitment and enables the acquisition of primitive endoderm fate. *Development* **149**, dev201074 (2022).
45. Martello, G. et al. Esrrb is a pivotal target of the Gsk3/Tcf3 axis regulating embryonic stem cell self-renewal. *Cell Stem Cell* **11**, 491–504 (2012).
46. Gassler, J. et al. Zygotic genome activation by the totipotency pioneer factor Nr5a2. *Science* **378**, 1305–1315 (2022).
47. Maskalenka, K. et al. NANOGP1, a tandem duplicate of NANOG, exhibits partial functional conservation in human naïve pluripotent stem cells. *Development* **150**, dev201155 (2023).
48. Domcke, S. et al. A human cell atlas of fetal chromatin accessibility. *Science* **370**, eaba7612 (2020).
49. Evseenko, D. et al. Mapping the first stages of mesoderm commitment during differentiation of human embryonic stem cells. *Proc. Natl. Acad. Sci. USA* **107**, 13742–13747 (2010).
50. Bernardo, A. S. et al. BRACHYURY and CDX2 mediate BMP-induced differentiation of human and mouse pluripotent stem cells into embryonic and extraembryonic lineages. *Cell Stem Cell* **9**, 144–155 (2011).
51. Allshire, R. C. & Madhani, H. D. Ten principles of heterochromatin formation and function. *Nat. Rev. Mol. Cell Biol.* **19**, 229–244 (2018).
52. Pontis, J. et al. Hominoid-specific transposable elements and KZFPs facilitate human embryonic genome activation and control transcription in naive human ESCs. *Cell Stem Cell* **24**, 724–735.e5 (2019).
53. Wu, F. et al. Species-specific rewiring of definitive endoderm developmental gene activation via endogenous retroviruses through TET1-mediated demethylation. *Cell Rep.* **41**, 111791 (2022).
54. Macfarlan, T. S. et al. Embryonic stem cell potency fluctuates with endogenous retrovirus activity. *Nature* **487**, 57–63 (2012).
55. Pontis, J. et al. Primate-specific transposable elements shape transcriptional networks during human development. *Nat. Commun.* **13**, 7178 (2022).
56. Wang, H. et al. SVA elements: a hominid-specific retroposon family. *J. Mol. Biol.* **354**, 994–1007 (2005).
57. Grow, E. J. et al. Intrinsic retroviral reactivation in human preimplantation embryos and pluripotent cells. *Nature* **522**, 221–225 (2015).
58. Theunissen, T. W. et al. Molecular criteria for defining the naive human pluripotent state. *Cell Stem Cell* **19**, 502–515 (2016).
59. Khan, H., Smit, A. & Boissinot, S. Molecular evolution and tempo of amplification of human LINE-1 retrotransposons since the origin of primates. *Genome Res* **16**, 78–87 (2006).
60. Hazra, D., Andrić, V., Palancade, B., Rougemaille, M. & Graille, M. Formation of S. pombe Erh1 homodimer mediates gametogenic gene silencing and meiosis progression. *Sci. Rep.* **10**, 1034 (2020).
61. Hazra, D., Chapat, C. & Graille, M. m^{6}A mRNA destiny: chained to the rhYTHm by the YTH-containing proteins. *Genes* **10**, E49 (2019).

62. Liao, S., Sun, H. & Xu, C. YTH domain: a family of N6-methyladenosine (m6A) Readers. *Genomics Proteom. Bioinforma.* **16**, 99–107 (2018).
63. Liu, J. et al. The RNA m(6)A reader YTHDC1 silences retrotransposons and guards ES cell identity. *Nature* **591**, 322–326 (2021).
64. Sun, T. et al. Crosstalk between RNA m6A and DNA methylation regulates transposable element chromatin activation and cell fate in human pluripotent stem cells. *Nat. Genet* **55**, 1324–1335 (2023).
65. Drakouli, S., Lyberopoulou, A., Papathanassiou, M., Mylonis, I. & Georgatsou, E. Enhancer of rudimentary homologue interacts with scaffold attachment factor B at the nuclear matrix to regulate SR protein phosphorylation. *FEBS J.* **284**, 2482–2500 (2017).
66. Maison, C. et al. Higher-order structure in pericentric heterochromatin involves a distinct pattern of histone modification and an RNA component. *Nat. Genet.* **30**, 329–334 (2002).
67. Xu, W. et al. METTL3 regulates heterochromatin in mouse embryonic stem cells. *Nature* **591**, 317–321 (2021).
68. Huo, X. et al. The nuclear matrix protein SAFB cooperates with major satellite RNAs to stabilize heterochromatin architecture partially through phase separation. *Mol. Cell* **77**, 368–383 e7 (2020).
69. Obersriebnig, M. J., Pallesen, E. M. H., Sneppen, K., Trusina, A. & Thon, G. Nucleation and spreading of a heterochromatic domain in fission yeast. *Nat. Commun.* **7**, 11518 (2016).
70. Murawska, M. et al. The histone chaperone FACT facilitates heterochromatin spreading by regulating histone turnover and H3K9 methylation states. *Cell Rep.* **37**, 109944 (2021).
71. Greenstein, R. A. et al. Noncoding RNA-nucleated heterochromatin spreading is intrinsically labile and requires accessory elements for epigenetic stability. *Elife* **7**, 32948 (2018).
72. Hornbeck, P. V. et al. PhosphoSitePlus, 2014: mutations, PTMs and recalibrations. *Nucleic Acids Res.* **43**, D512–D520 (2015).
73. Al Adhami, H. et al. Systematic identification of factors involved in the silencing of germline genes in mouse embryonic stem cells. *Nucleic Acids Res.* **51**, gkad071 (2023) https://doi.org/10.1093/nar/gkad071.
74. Wu, D. & Dean, J. RNA exosome ribonuclease DIS3 degrades Pou6f1 to promote mouse pre-implantation cell differentiation. *Cell Rep.* **42**, 112047 (2023).
75. Imamura, K. et al. A functional connection between the microprocessor and a variant NEXT complex. *Mol. Cell* **84**, 4158–4174.e6 (2024).
76. Yang, P., Wang, Y. & Macfarlan, T. S. The Role of KRAB-ZFPs in transposable element repression and mammalian evolution. *Trends Genet.* **33**, 871–881 (2017).
77. Imbeault, M., Helleboid, P.-Y. & Trono, D. KRAB zinc-finger proteins contribute to the evolution of gene regulatory networks. *Nature* **543**, 550–554 (2017).
78. Skene, P. J. & Henikoff, S. An efficient targeted nuclease strategy for high-resolution mapping of DNA binding sites. *Elife* **6**, e21856 (2017).
79. Katznelson, A. & Zaret, K. A fluorescence-based protocol to quantitatively titrate CUT&RUN buffer components. *STAR Protoc.* **5**, 102866 (2024).
80. Liu, N. et al. Direct promoter repression by BCL11A controls the fetal to adult hemoglobin switch. *Cell* **173**, 430–442.e17 (2018).
81. Langmead, B. & Salzberg, S. L. Fast gapped-read alignment with Bowtie 2. *Nat. Methods* **9**, 357–359 (2012).
82. Jin, H. et al. ChIPseqSpikeInFree: a ChIP-seq normalization approach to reveal global changes in histone modifications without spike-in. *Bioinformatics* **36**, 1270–1272 (2020).
83. Meers, M. P., Tenenbaum, D. & Henikoff, S. Peak calling by sparse enrichment analysis for CUT&RUN chromatin profiling. *Epigenetics Chromatin* **12**, 42 (2019).
84. Heinz, S. et al. Simple combinations of lineage-determining transcription factors prime cis-regulatory elements required for macrophage and B cell identities. *Mol. cell* **38**, 576–589 (2010).
85. Ramírez, F. et al. deepTools2: a next generation web server for deep-sequencing data analysis. *Nucleic Acids Res.* **44**, W160–W165 (2016).
86. Khan, A. & Mathelier, A. Intervene: a tool for intersection and visualization of multiple gene or genomic region sets. *BMC Bioinforma.* **18**, 287 (2017).
87. Dobin, A. et al. STAR: ultrafast universal RNA-seq aligner. *Bioinformatics* **29**, 15–21 (2013).
88. Liao, Y., Smyth, G. K. & Shi, W. featureCounts: an efficient general purpose program for assigning sequence reads to genomic features. *Bioinformatics* **30**, 923–930 (2014).
89. Jin, Y., Tam, O. H., Paniagua, E. & Hammell, M. TEtranscripts: a package for including transposable elements in differential expression analysis of RNA-seq datasets. *Bioinformatics* **31**, 3593–3599 (2015).
90. Love, M. I., Huber, W. & Anders, S. Moderated estimation of fold change and dispersion for RNA-seq data with DESeq2. *Genome Biol.* **15**, 550 (2014).
91. Filippi-Chiela, E. C. et al. Nuclear morphometric analysis (NMA): screening of senescence, apoptosis and nuclear irregularities. *PLoS One* **7**, e42522 (2012).
92. Thomas, P. D. et al. PANTHER: making genome-scale phylogenetics accessible to all. *Protein Sci.* **31**, 8–22 (2022).
93. Cao, J. et al. A human cell atlas of fetal gene expression. *Science* **370**, eaba7721 (2020).

Author contributions

Conceptualization, R.L.M. and K.Z.; Formal analysis, A.K., B.H., H.F., K.T. and R.L.M.; Funding acquisition, K.Z; Investigation, A.K., B.H., H.F., K.T., J.Z., A.B. and R.L.M.; Methodology, A.K., B.H., R.L.M. and K.Z.; Project administration, R.L.M and K.Z.; Resources, R.L.M. and K.Z.; Supervision, M.T-P., N.P., R.L.M. and K.Z.; Writing – Original Draft, A.K., R.L.M. and K.Z.

Funding

R.L.M. was supported by an NIH NIDDK K01 postdoctoral fellowship DK117970-01 and by NIDDK (DK144249-01A1). N.P. was supported by NIGMS (GM139970-01) and NICHD (HD102013-01A1). R35GM153180 supported work in the lab of K.S.Z.

Competing interests

The authors declare no competing interests.

Additional information

Supplementary information The online version contains supplementary material available at https://doi.org/10.1038/s41467-026-76015-3.

Correspondence and requests for materials should be addressed to Kenneth S. Zaret or Ryan L. McCarthy.

Peer review information *Nature Communications* thanks the anonymous reviewer(s) for their contribution to the peer review of this work. A peer review file is available.

Reprints and permissions information is available at http://www.nature.com/reprints

Publisher's note Springer Nature remains neutral with regard to jurisdictional claims in published maps and institutional affiliations.

Open Access This article is licensed under a Creative Commons Attribution-NonCommercial-NoDerivatives 4.0 International License, which permits any non-commercial use, sharing, distribution and reproduction in any medium or format, as long as you give appropriate credit to the original author(s) and the source, provide a link to the Creative Commons licence, and indicate if you modified the licensed material. You do not have permission under this licence to share adapted material derived from this article or parts of it. The images or other third party material in this article are included in the article's Creative Commons licence, unless indicated otherwise in a credit line to the material. If material is not included in the article's Creative Commons licence and your intended use is not permitted by statutory regulation or exceeds the permitted use, you will need to obtain permission directly from the copyright holder. To view a copy of this licence, visit http://creativecommons.org/licenses/by-nc-nd/4.0/.

© The Author(s) 2026